

⁸⁸Sr Reference Data

Sebastian Pucher^{1,2†} Sofus Laguna Kristensen^{1,2‡} Ronen M. Kroeze^{2,3*}

¹Max-Planck-Institut für Quantenoptik, 85748 Garching, Germany

²Munich Center for Quantum Science and Technology, 80799 München, Germany

³Fakultät für Physik, Ludwig-Maximilians-Universität, 80799 München, Germany

(Dated: July 15, 2025)

Strontium-88 is a versatile atomic species often used in quantum optics, precision metrology, and quantum computing. Consolidated atomic data is essential for the planning, execution, and evaluation of experiments. In this reference, we present physical and optical properties of neutral ⁸⁸Sr relevant to these applications. Here we focus on experimental results and supplement these with theoretical values. We present equations to convert values and derive important parameters. Tabulated results include key parameters for commonly used transitions in ⁸⁸Sr (¹S₀ → ¹P₁, ¹S₀ → ³P_{0,1,2}, and ³P_{0,1,2} → ³S₁). This dataset serves as an up-to-date reference for studies involving bosonic ⁸⁸Sr.

1 Introduction

In this reference, we present the physical and optical properties of strontium-88 (⁸⁸Sr) relevant to various quantum optics, laser cooling, and precision measurement experiments. This document is inspired by the widely used references on alkali atoms by Daniel A. Steck [1–4]. Our goal is to provide experimentalists and theorists with consolidated data and calculated parameters that are important for understanding the interaction of light with strontium atoms.

We consider the relevant electronic level structure of ⁸⁸Sr, in the context of laser cooling, optical trapping, coherent manipulation, and optical clock operation. In particular, we summarize the following optical transitions:

- The broad, dipole-allowed $5s^2\ ^1S_0 \rightarrow 5s5p\ ^1P_1$ transition at a wavelength λ of about 461 nm, which is used for first-stage laser cooling and Zeeman slowing (blue MOT transition), but also commonly for atomic imaging schemes.
- The narrow spin-forbidden intercombination $5s^2\ ^1S_0 \rightarrow 5s5p\ ^3P_1$ transition at $\lambda \approx 698$ nm, used for second-stage cooling to sub-microkelvin temperatures (red MOT transition).
- The additional dipole-allowed transitions at $\lambda \approx 679$ nm, 688 nm, and 707 nm are used to excite atoms into the $5s6s\ ^3S_1$ state, which is primarily used to manipulate and repump population of the long-lived metastable $5s5p\ ^3P_0$ and $5s5p\ ^3P_2$ states back into the cooling cycle.
- The ultra-narrow $5s^2\ ^1S_0 \rightarrow 5s5p\ ^3P_0$ transition at $\lambda \approx 698$ nm, used in optical lattice clocks for precision timekeeping and as an optical qubit for quantum information applications.
- The ultra-narrow $5s^2\ ^1S_0 \rightarrow 5s5p\ ^3P_2$ transition at $\lambda \approx 671$ nm, relevant for state preparation, manipulation, and quantum simulations.

Measured values are provided with their corresponding references to original experimental sources, while calculated quantities are derived using established physical models, with citations to more detailed theoretical discussions. The data provided here are not guaranteed to be complete or error-free. For parameters critical to your research, you should consult the primary literature.

This document is intended as a community resource, following the example of Steck’s *Alkali D Line Data* series, available at <http://steck.us/alkalidata>. We hope that this summary will serve experimental and theoretical researchers working with strontium, whether for atomic physics, quantum simulation, or frequency metrology. Comments, corrections, and suggestions for improving this document are welcomed and encouraged.

[†] Email: sebastian.pucher@protonmail.com

[‡] Email: sofus.kristensen@mpq.mpg.de

^{*} Email: r.kroeze@lmu.de

2 Statistics Introduction

This section outlines the statistical methods used to combine and report the numerical values derived from multiple experimental or theoretical sources. If more than one value is cited for quantities such as the transition frequency, the lifetime of a state, the isotope shift, or the scattering length, the quoted value is a weighted mean of the values from the references, calculated as

$$\mu = \frac{\sum_{j=1}^n x_j / \sigma_j^2}{\sum_{j=1}^n 1 / \sigma_j^2}, \quad (1)$$

where x_j are the measurement values with uncertainties σ_j , and $(j = 1, \dots, n)$ indexes the individual references. Here, the weights are the inverse squares of the uncertainties. The corresponding standard uncertainty in the weighted mean is

$$\sigma_\mu = \sqrt{\frac{1}{\sum_{j=1}^n 1 / \sigma_j^2}}. \quad (2)$$

If the measurements are not statistically consistent (i.e., the scatter exceeds what is expected from the reported uncertainties), we scale the uncertainty in the mean by the Birge ratio [5], defined as

$$R_B = \sqrt{\frac{1}{n-1} \sum_{j=1}^n \frac{(x_j - \mu)^2}{\sigma_j^2}} = \sqrt{\frac{\chi^2}{n-1}}, \quad (3)$$

where χ^2 is the chi-squared value and n is the number of data points. The final uncertainty in the mean is then

$$\sigma_\mu^{\text{adj}} = R_B \cdot \sigma_\mu. \quad (4)$$

If $R_B > 1$ for one dataset, we show R_B next to the reported weighted mean to indicate that the measured values are statistically inconsistent, and we adjusted the uncertainty with the Birge ratio. We note that alternative techniques for assessing the uncertainty of a weighted mean are actively being investigated and may be employed in future updates [6].

When an experimental reference reports both a statistical uncertainty σ_{stat} and a systematic uncertainty σ_{sys} for a single measurement, the uncertainties are assumed to be uncorrelated. Hence, we combine the two contributions in quadrature to give the total one-sigma uncertainty

$$\sigma = \sqrt{\sigma_{\text{stat}}^2 + \sigma_{\text{sys}}^2}. \quad (5)$$

In cases where only asymmetric limits are provided, e.g. $x_0^{+\Delta x_+}_{-\Delta x_-}$, we obtain a single symmetric uncertainty by taking the larger deviation

$$\sigma = \max(\Delta x_+, \Delta x_-). \quad (6)$$

Reporting $x_0(\sigma) = x_0 \pm \sigma$ then guarantees coverage of both published bounds. Although this approach overestimates the error when the true distribution is asymmetric, it provides a straightforward, conservative uncertainty for tables and figures.

3 Strontium Properties

Strontium is a soft, silver-white alkaline-earth metal. Freshly cut, it displays a bright silvery luster that quickly turns yellow as surface oxide forms. Below 380 °C, it does not absorb nitrogen, but it should be stored in, e.g., mineral oil or an argon atmosphere to prevent oxidation [7]. Strontium reacts vigorously with water [7]. Contaminated parts and tools can be cleaned with water to remove unwanted strontium, but this should be done with caution due to the rapid reaction of the metal with water. In finely divided form, the metal can spontaneously ignite in air [7].

Strontium has 38 electrons, two of which occupy the outermost shell. Natural strontium consists of the four stable isotopes ^{84}Sr , ^{86}Sr , ^{87}Sr , and ^{88}Sr , alongside more than thirty known unstable isotopes. This review focuses on the most abundant stable isotope ^{88}Sr .

Table 1 lists selected fundamental physical constants from the 2022 CODATA recommended values that we use in this reference [8]. In Table 2, key physical properties of the isotope ^{88}Sr are summarized. For this isotope, the nuclear spin vanishes resulting in bosonic particle statistics. The mass is the recommended value from the 2020

Atomic Mass Evaluation (AME2020) [9, 10]. The value is based on measurements of cyclotron frequency ratios of ion pairs simultaneously confined in a Penning trap [11].

The relative natural abundance, the specific heat capacity, and the molar heat capacity are taken from Ref. [7]. The density and molar volume at various temperatures can be found in Ref. [12]. The vapor pressure at a temperature of $T = 25^\circ\text{C}$, as well as the temperature-dependent vapor pressure curve shown in Figure 1, are calculated using the semi-empirical equation describing solid strontium provided by [13]

$$\log_{10}(P) = 9.226 + \log_{10}(101325) - \frac{8572}{T} - 1.1926 \log_{10}(T) , \quad (7)$$

where P is the vapor pressure in pascals and T is the temperature in Kelvin. This equation is valid from $T = 298\text{ K}$ up to the melting point of strontium, reported as $T_M = 1050\text{ K}$ (777°C) [7]. In this range, it reproduces the experimental vapor pressure with an accuracy better than $\pm 5\%$ [13]. Note that the density, the molar volume, the melting and boiling points, the heat capacities, as well as the vapor pressure are given for the naturally occurring form of Sr. Using its natural isotopic abundance, the corresponding values for ^{88}Sr can be inferred.

The s -wave scattering length a characterizes low-energy elastic collisions between atoms and plays a central role in ultracold gas experiments [14]. Its magnitude governs the rate of thermalization during evaporative cooling. The sign of the scattering lengths determines whether the interactions are repulsive and a Bose–Einstein condensate (BEC) is stable (for $a > 0$) or the interactions are attractive and the BEC is prone to collapse (for $a < 0$) [15]. In alkali atoms, a can be magnetically tuned via Feshbach resonances to nearly arbitrary values $(-\infty, +\infty)$ [15]. In contrast, alkaline-earth atoms such as Sr have a $J = 0$ ground state, making them largely insensitive to magnetic tuning. For these systems, the scattering length is given by the binding energy of the highest vibrational state of the ground-state molecular potential, which shifts slightly with isotopic mass [16]. However, Feshbach resonances can exist in a cold-atom ensemble of mixtures of the ground state $^1\text{S}_0$ and metastable state $^3\text{P}_1$, as shown in Yb [17]. The isotope considered in this reference, ^{88}Sr , has a small scattering length (see Tab. 3), resulting in a low elastic collision rate. This makes evaporative cooling practically impossible, but is very beneficial for precision measurements [16].

For potentials that decay faster than $1/r^3$ as $r \rightarrow \infty$, the scattering length is defined as the following low-energy limit

$$\lim_{k \rightarrow 0} k \cot \delta(k) = -\frac{1}{a} , \quad (8)$$

where k is the wave number and $\delta(k)$ is the phase shift of the outgoing spherical wave. Moreover, the elastic cross section σ_e , at sufficiently low energies, is related to the scattering length via

$$\lim_{k \rightarrow 0} \sigma_e = 4\pi a^2 . \quad (9)$$

4 Level Structure

As an alkaline-earth atom, Sr has two valence electrons, giving rise to a level structure of singlet and triplet terms, analogous to helium. Figure 2 shows the energy levels and transitions discussed in this reference, while Figure 4 places them within the complete Sr I level scheme. Similar level schemes can be found, e.g., in Refs. [18, 19]. The electronic configuration features both broad electric-dipole-allowed transitions with linewidths on the order of megahertz and narrow intercombination lines between singlet and triplet manifolds, with natural linewidths spanning millihertz to kilohertz.

The atomic-level notation generally consists of two parts: the electronic configuration and the term symbol $^{2S+1}L_J$. For the configuration, a sequence such as $n_1 l_1 n_2 l_2 \dots$ indicates which orbitals are occupied by the valence electrons. For example, $5s5p$ means that one electron is in the $5s$ shell and one in the $5p$ shell. In the term symbol, the superscript $2S + 1$ is the spin multiplicity, where S is the total spin quantum number ($2S + 1 = 1$ for singlet, $2S + 1 = 3$ for triplet). The letter L encodes the total orbital angular momentum (S for $L = 0$, P for $L = 1$, D for $L = 2$, ...). The subscript J is the quantum number corresponding to the total electronic angular momentum. Putting these together, a state labeled

$$n_1 l_1 n_2 l_2 \ ^{2S+1}L_J \quad (10)$$

specifies both which orbitals the valence electrons occupy and the combined spin and orbital angular momentum quantum numbers of the entire atom. In practice, when the configuration $n_1 l_1 n_2 l_2$ is unambiguous from context, we omit the explicit $n_1 l_1 n_2 l_2$ prefix and simply write the term symbol $^{2S+1}L_J$ for better readability.

4.1 Energy Level Splittings

In ^{88}Sr , each electronic term is split by spin-orbit (fine-structure) interactions into levels of different J . The total electronic angular momentum \mathbf{J} arises from coupling the orbital (\mathbf{L}) and spin (\mathbf{S}) angular momenta of the two valence electrons

$$\mathbf{J} = \mathbf{L} + \mathbf{S}. \quad (11)$$

Here, the magnitude of \mathbf{J} is given by $\sqrt{J(J+1)}\hbar$ with possible integer values of J in the range

$$|L - S| \leq J \leq L + S. \quad (12)$$

Accordingly, the $5s^2\ ^1\text{S}_0$ ground state of ^{88}Sr remains unsplit, while the lowest excited term $5s5p\ ^3\text{P}$ splits into the $^3\text{P}_0$, $^3\text{P}_1$, and $^3\text{P}_2$ fine-structure levels.

Hyperfine structure results from the interaction of \mathbf{J} with the nuclear spin given by the total nuclear angular momentum \mathbf{I} resulting in the total atomic angular momentum

$$\mathbf{F} = \mathbf{J} + \mathbf{I}, \quad (13)$$

where

$$|J - I| \leq F \leq J + I. \quad (14)$$

However, ^{88}Sr has nuclear spin $I = 0$. As a result, its level structure exhibits only fine-structure splittings, without the additional multiplet substructure seen in fermionic isotopes. Consequently, all hyperfine constants, the magnetic dipole A , electric quadrupole B , magnetic octupole C , etc., vanish for this isotope.

4.2 Interaction with Magnetic Fields

The interaction between static external fields and ^{88}Sr produces energy shifts and state couplings that are central in precision-metrology, quantum-simulation, and quantum computing protocols. In this section, we first examine how a static magnetic field lifts the degeneracy of the m_J sublevels via the Zeeman effect. Then, we discuss state mixing, both intrinsic (spin-orbit) and externally induced, which enables otherwise forbidden transitions.

4.2.1 Zeeman Effect

In ^{88}Sr , which has no nuclear spin and thus no hyperfine structure, atomic energy levels are characterized by their total electronic angular momentum J . Each state with angular momentum J contains $2J + 1$ magnetic sublevels corresponding to the magnetic quantum number m_J , describing the projection of \mathbf{J} along the quantization axis.

In the absence of an external magnetic field, these m_J sublevels are energetically degenerate. When a magnetic field is applied, this degeneracy is lifted due to the Zeeman effect. The Hamiltonian describing the interaction of the atomic electrons with a static magnetic field \mathbf{B} , aligned along the z -axis which defines the quantization axis, is

$$H_B = \frac{\mu_B}{\hbar} (g_S \mathbf{S} + g_L \mathbf{L}) \cdot \mathbf{B} = \frac{\mu_B}{\hbar} (g_S S_z + g_L L_z) B_z, \quad (15)$$

where μ_B is the Bohr magneton, g_S and g_L are the electron spin and orbital g -factors respectively, and S_z and L_z are the spin and orbital angular momentum components along the z -axis.

The value for g_S has been measured precisely, and we list the CODATA recommended value in Tab. 2. The orbital g -factor can be corrected for finite nuclear mass by [20]

$$g_L = 1 - \frac{m_e}{m_{\text{nuc}}}, \quad (16)$$

where m_e is the electron mass and m_{nuc} is the nuclear mass, accurate to leading order in m_e/m_{nuc} .

When the energy shifts due to the magnetic field are small compared to the fine-structure splitting, J remains a good quantum number and the Hamiltonian simplifies to

$$H_B = \frac{\mu_B}{\hbar} g_J J_z B_z. \quad (17)$$

Here, the Landé g -factor g_J is given by

$$g_J = g_L \frac{J(J+1) - S(S+1) + L(L+1)}{2J(J+1)} + g_S \frac{J(J+1) + S(S+1) - L(L+1)}{2J(J+1)}. \quad (18)$$

Using $g_S \approx 2$ and $g_L \approx 1$, g_J can be approximated as

$$g_J \approx 1 + \frac{J(J+1) + S(S+1) - L(L+1)}{2J(J+1)} . \quad (19)$$

Note that the expression here does not include corrections due to the complicated multi-electron structure [20]. The operator J_z in Eq. 17 acts as

$$J_z |J, m_J\rangle = \hbar m_J |J, m_J\rangle . \quad (20)$$

Hence, to first order, the energy shift for each Zeeman sublevel is

$$\Delta E_{J, m_J} = \langle J, m_J | H_B | J, m_J \rangle = \frac{\mu_B}{\hbar} g_J (\hbar m_J) B_z = \mu_B g_J m_J B_z . \quad (21)$$

The corresponding frequency shift is

$$\Delta\omega = \frac{\Delta E}{\hbar} = \frac{\mu_B}{\hbar} g_J m_J B_z . \quad (22)$$

This linear Zeeman effect leads to an equal spacing between adjacent magnetic sublevels, proportional to the magnetic field strength and the state's g_J factor. These shifts play a central role in magneto-optical trapping, laser spectroscopy, and atomic clock operation using strontium.

4.2.2 State Mixing

In bosonic ^{88}Sr , there is no hyperfine interaction to mix states. All state mixing arises from spin-orbit coupling in the $5s5p$ manifold. The mixing can be described using the methods in Refs. [21–23]. The physical states $^{2S+1}L_J$ are written as admixtures of pure spin-orbit coupling states $^{2S+1}L_J^{(0)}$ [23]:

$$\begin{pmatrix} |^1P_1\rangle \\ |^3P_0\rangle \\ |^3P_1\rangle \\ |^3P_2\rangle \end{pmatrix} = \begin{pmatrix} \alpha & 0 & -\beta & 0 \\ 0 & 1 & 0 & 0 \\ \beta & 0 & \alpha & 0 \\ 0 & 0 & 0 & 1 \end{pmatrix} \begin{pmatrix} |^1P_1^{(0)}\rangle \\ |^3P_0^{(0)}\rangle \\ |^3P_1^{(0)}\rangle \\ |^3P_2^{(0)}\rangle \end{pmatrix} . \quad (23)$$

with $\alpha^2 + \beta^2 = 1$. For Sr one finds $\alpha \approx 0.9996$ and $\beta \approx -0.0286$ [23]. Hence, the $|^3P_1\rangle$ state carries a $\beta^2 \approx 0.08\%$ singlet admixture. The ground state $|^1S_0\rangle$ is pure singlet state, and electric-dipole (E1) selection rules would forbid a direct $^1S_0 \rightarrow ^3P_J$ transition if the excited states were pure. However, since

$$\langle ^1S_0 | \hat{\mathbf{d}} | ^3P_1 \rangle = \beta \langle ^1S_0 | \hat{\mathbf{d}} | ^1P_1^{(0)} \rangle \neq 0 , \quad (24)$$

the 689 nm intercombination transition becomes weakly allowed with a spontaneous decay rate $\propto \beta^2$, yielding the long lifetime τ_{3P_1} . Here, $\hat{\mathbf{d}}$ is the dipole operator.

The $^1S_0 \rightarrow ^3P_0$ clock transition is strictly forbidden except via a two-photon E1M1 process, giving an intrinsic lifetime of order 10^3 years [24]. More generally, one can relate the 3P_0 lifetime to that of 3P_1 by [25]

$$\tau_{3P_0} = \left(\frac{\omega_{3P_1}}{\omega_{3P_0}} \right)^3 \frac{\beta^2}{(\tilde{\alpha}_0 \beta + \tilde{\beta}_0 \alpha)^2} \tau_{3P_1} , \quad (25)$$

where $\tilde{\alpha}_0, \tilde{\beta}_0$ are the hyperfine-mixing coefficients. In bosonic ^{88}Sr , $\tilde{\alpha}_0 = \tilde{\beta}_0 = 0$, so the denominator vanishes and $\tau_{3P_0} \rightarrow \infty$ (i.e. $\sim 10^3$ yr), making the clock line unusable without external mixing.

Several proposals to realize such a mixing can be found in the literature, see e.g. discussion in Ref. [25]. To make the $^1S_0 \rightarrow ^3P_0$ transition usable, a static magnetic field B can be applied to mix the $|^3P_0\rangle$ state with $|^3P_1\rangle$ state via the magnetic-dipole operator $\hat{\mu}$ [26]

$$|^3P'_0\rangle = |^3P_0\rangle + \frac{\langle ^3P_1 | \hat{\mu} \cdot B | ^3P_0 \rangle}{\Delta_{10}} |^3P_1\rangle , \quad (26)$$

where $\Delta_{10} \equiv \omega_{3P_1} - \omega_{3P_0} \approx 2\pi \times 5.6$ THz, see values in Tab. 7 and Tab. 11. Since $|^3P_1\rangle$ itself carries the small β -admixture of $|^1P_1\rangle$, the doubly-mixed clock state becomes

$$|^3P'_0\rangle = |^3P_0\rangle + \frac{\langle ^3P_1 | \hat{\mu} \cdot B | ^3P_0 \rangle}{\Delta_{10}} (\alpha |^3P_1^{(0)}\rangle + \beta |^1P_1^{(0)}\rangle) . \quad (27)$$

The singlet component gives the otherwise forbidden $^1S_0 \rightarrow ^3P_0$ transition a nonzero E1 matrix element. The Hamiltonian in Eq. 15 has no first-order energy shift on the clock state $|^3P_0\rangle$, but it mixes it with the $|^3P_1, m_J = 0\rangle$ state. This magnetic admixture induces a small but finite decay rate for the dressed clock state to the ground state [27]

$$\Gamma_{\text{clock}}(\mathbf{B}) = \Gamma_{3P1} \cdot \frac{\mu_C^2 \mathbf{B}^2}{2\Delta_{10}^2}, \quad (28)$$

where $\mu_C \equiv \sqrt{\frac{2}{3}}(g_L - g_S)\mu_B$. Even for strong fields $|\mathbf{B}| \approx 1000 \text{ G}$, the induced linewidth remains narrow, e.g., $\Gamma_{\text{clock}} \approx 2\pi \times 0.3 \text{ mHz}$ (i.e. $\tau \approx 530 \text{ s}$) [27]. This magnetic mechanism is essential for enabling precision spectroscopy on the bosonic clock transition. Notably, the same transition in fermionic ^{87}Sr is weakly allowed even at $B = 0$ due to hyperfine-induced state mixing, which can be understood as an effective internal magnetic field arising from the nonzero nuclear spin $I = 9/2$.

5 Transition Properties

This section examines the key atomic transitions. Measured transition frequencies are presented and converted to wavelengths and transition energies. Experimentally determined lifetimes of the excited states are reviewed. Equations for obtaining additional parameters from these transition data and lifetimes are introduced.

5.1 Transition Frequencies and Wavelengths

The following relations allow one to convert a transition frequency $\omega_0 = 2\pi \times \nu$ to the corresponding transition energy, vacuum wavelength, air wavelength, and wavenumber. The photon energy E is

$$E = h\nu = \hbar\omega_0. \quad (29)$$

This transition energy can be converted into an energy in eV using

$$E_{\text{eV}} = \frac{h\nu}{e} = \frac{\hbar\omega_0}{e}. \quad (30)$$

The vacuum wavelength λ and the angular wavenumber k_L are

$$\lambda = \frac{c}{\nu} = \frac{2\pi c}{\omega_0}, \quad (31)$$

$$k_L = \frac{2\pi}{\lambda} = \frac{\omega_0}{c}. \quad (32)$$

The wavelength in air is given by

$$\lambda_{\text{air}} = \frac{\lambda}{n_{\text{air}}}, \quad (33)$$

where n_{air} is the refractive index of air. To compute the refractive index of air under typical laboratory conditions, the Edlén's equation is a common approximation [28, 29]

$$n_{\text{air}} = 1 + \left[\left(8342.54 + \frac{2406.147}{130 - \kappa^2} + \frac{15.998}{38.9 - \kappa^2} \right) \frac{P}{96\,095.43} \frac{1 + 10^{-8}(0.601 - 0.00972T)P}{1 + 0.0036610T} - f(0.037345 - 0.000401\kappa^2) \right] \times 10^{-8}, \quad (34)$$

where $\kappa = k_L/(2\pi)$ is the vacuum wavenumber in μm^{-1} , P is the total air pressure in Pa, T is the temperature in $^\circ\text{C}$, f is the partial pressure of water vapor in Pa (obtainable from relative humidity via the Buck equation [30, 31]). Under standard conditions ($P = 101\,325 \text{ Pa}$, $T = 25^\circ\text{C}$, 50% relative humidity), this yields $n_{\text{air}} \approx 1.00027$ in the visible range with a 1σ uncertainty of 1×10^{-8} which has been used throughout this reference. In real-world applications, additional uncertainties due to fluctuations in pressure, temperature, and humidity must be considered and are not included here, see e.g. [1–4].

We now review the experimental measurements of the transition frequencies that we present in this work. To date, no high-precision measurement of the $^1S_0 \rightarrow ^1P_1$ (blue MOT) transition frequency has been found. We therefore adopt the value quoted in a 2010 review [32], which in turn is based on an measurement from 1936 [33]. Accurate frequency measurements of the $^1S_0 \rightarrow ^3P_1$, $^3P_1 \rightarrow ^3S_1$, and $^3P_0 \rightarrow ^3S_1$ transitions were performed in 2005 [34]. The absolute frequency of the $^1S_0 \rightarrow ^3P_0$ clock transition in ^{88}Sr was experimentally measured and

we obtain a weighted mean value of 429 228 066 418 008(2) Hz [35, 36]. However, in Tab. 11, we adopt the value from the 2021 CIPM recommendation published by the BIPM [37], which is endorsed by the CCTF as a secondary representation of the SI second [38]. The absolute frequency of the magnetic quadrupole transition $^1\text{S}_0 \rightarrow ^3\text{P}_2$ at $\lambda \approx 671$ nm was measured using cold atoms trapped in a lattice and an optical frequency comb [39].

For the repump transition $^3\text{P}_2 \rightarrow ^3\text{S}_1$, we infer the transition frequency in ^{88}Sr from a measurement performed on the isotope ^{87}Sr . Specifically, we use the measured transition frequency ν_{87} between the hyperfine levels $^3\text{P}_2(F = \frac{7}{2}) \rightarrow ^3\text{S}_1(F = \frac{7}{2})$ in ^{87}Sr , reported in 2019 [40]. To convert this frequency to the corresponding transition frequency in ^{88}Sr , we first obtain the center-of-gravity frequency of the transition ν_{87}^{CG} by removing the hyperfine shifts of the lower state $\Delta_{3\text{P}_2(F=7/2)} = 1597.138(8)$ MHz [41] and the upper state $\Delta_{3\text{S}_1(F=7/2)} = 2981.0(6)$ MHz [34]

$$\nu_{87}^{\text{CG}} = \nu_{87} - [\Delta_{3\text{P}_2(F=7/2)} - \Delta_{3\text{S}_1(F=7/2)}]. \quad (35)$$

Then, we subtract the isotope shifts for the two levels, $\delta_{\text{iso},3\text{S}_1}$ [34] and $\delta_{\text{iso},3\text{P}_2}$ [39], yielding the corresponding transition frequency in ^{88}Sr

$$\nu_{88} = \nu_{87}^{\text{CG}} + [\delta_{\text{iso},3\text{S}_1} - \delta_{\text{iso},3\text{P}_2}]. \quad (36)$$

All strontium isotopes share the same electronic level structure, but differences in nuclear mass and charge distribution shift their optical transition frequencies. The mass-dependent and volume-dependent contributions combine to yield the total isotope shift for each line. The transition Tabs. 6-12 compile published values of the isotope shift among the four stable Sr isotopes relative to ^{88}Sr . Since ^{87}Sr has a hyperfine structure, we present the shifts for the center-of-gravity frequency of the transitions.

5.2 Decay of Excited States

An excited state $|e\rangle$ that decays to several lower levels $\{|g_i\rangle\}$ is described by Einstein A -coefficients $A_{e \rightarrow g_i}$. The total spontaneous decay rate is

$$\Gamma = \sum_i A_{e \rightarrow g_i}. \quad (37)$$

The excited-state lifetime τ is directly related to the total spontaneous decay rate

$$\tau = \frac{1}{\Gamma}. \quad (38)$$

The corresponding full-width at half-maximum of the transition's line shape is

$$\Delta\nu_{\text{FWHM}} = \frac{\Gamma}{2\pi}. \quad (39)$$

Each decay channel i carries a branching ratio

$$\beta_i = \frac{A_{e \rightarrow g_i}}{\Gamma}, \quad (40)$$

so its partial decay rate is

$$\Gamma_{\text{partial}} = \beta_i \Gamma = A_{e \rightarrow g_i}. \quad (41)$$

Thus, combining a precise measurement of τ with known β_i directly yields the individual A -coefficients.

We now review experimental measurements and theoretical predictions of the lifetimes and branching ratios of relevant excited states in strontium. For the $^1\text{P}_1$ state, the lifetime has not been consistently determined. Two recent measurements agree within one standard deviation [42, 43]. In contrast, neither value overlaps within the stated errors with previous measurements [44–47]. Theoretically, a value of 5.234(8) ns [48] is predicted, which is in agreement with a measurement from 2005 [46]. The $^1\text{P}_1$ state decays with a theoretical branching ratio of 0.999 949 48(96) back to the $^1\text{S}_0$ ground state [48]. The dominant leakage channel from the excited state is the decay to the $^1\text{D}_2$ state, with a branching ratio of 1 : 20 538(342) [48], in agreement with an experimentally obtained value of 1 : 20 500(900) [49]. The lifetime of the $^1\text{D}_2$ state is 412(10) μs [50]. Historically, the branching ratio of its decay into the $^3\text{P}_1$ and $^3\text{P}_2$ states was estimated to be approximately 2 : 1 [51–53]. However, recent theoretical calculations [48] suggest that about 80.4(56) % of the atoms decay via the $^3\text{P}_1$ intermediate level back to the ground state and the remaining 19.6(56) % of the atoms decay to the metastable $^3\text{P}_2$ state.

Multiple independent studies have reported measurements of the $^3\text{P}_1$ excited-state lifetime [50, 54–57]. Except for the results in Ref. [50], all results agree within their quoted uncertainties. A recent measurement achieves a relative

precision well below one percent, representing the current benchmark for this lifetime [54]. For the lifetime of the $^3\text{S}_1$ state, four independent and inconsistent measurements were performed [42, 58–60]. The weighted mean of these lifetime values agrees with a recent theoretical calculation, which predicts a lifetime of 13.92(7) ns [48]. The $^3\text{S}_1$ state decays predominantly to the $^3\text{P}_{0,1,2}$ states, but there is a small leakage channel to the $^1\text{P}_1$ state with a branching ratio of $1.31(22) \times 10^{-4}$ [48].

The metastable $^3\text{P}_2$ state decays via a magnetic-quadrupole transition back to the ground state. The partial decay rate on this transition was recently measured [61]. However, faster processes, including magnetic-dipole decay into the nearby $^3\text{P}_1$ level and thermal (blackbody-induced) transfer to higher-lying triplet states, dominate under typical laboratory conditions. As a result, the measured total lifetime of the $^3\text{P}_2$ manifold is reduced to a few hundred seconds, reflecting the combined contributions of all available decay pathways [62, 63]. Additionally, Raman scattering processes induced by, e.g., trapping light fields can further shorten the effective lifetime.

5.3 Additional Transition Parameters

The spontaneous emission rate Γ determines the relative intensity of a spectral line. For a $J \rightarrow J'$ electric-dipole transition, Γ is directly linked to the absorption oscillator strength f via [64]

$$\Gamma = \frac{e^2 \omega_0^2}{2\pi\epsilon_0 m_e c^3} \frac{2J+1}{2J'+1} f. \quad (42)$$

A larger f (and hence larger Γ) implies a stronger, broader line. The spontaneous decay rate for a two-level atom is related to the dipole matrix element d via [65]

$$\Gamma = \frac{\omega_0^3 |d|^2}{3\pi\epsilon_0 \hbar c^3} \implies |d|^2 = \frac{3\pi\epsilon_0 \hbar c^3}{\omega_0^3} \Gamma. \quad (43)$$

If we want the line-specific moment d_i , we replace $\Gamma \rightarrow \Gamma_i = \beta_i \Gamma$, and find $|d_i|^2 = \beta_i |d|^2$. It is common to present reduced matrix elements $\langle J || e r || J' \rangle$, which are related to the dipole matrix element by the Wigner–Eckart theorem

$$\langle J || e r || J' \rangle = \sqrt{2J'+1} |d_i| = \sqrt{2J'+1} \sqrt{\frac{3\pi\epsilon_0 \hbar c^3}{\omega_0^3} \beta_i \Gamma}. \quad (44)$$

This expression is used to calculate the reduced matrix elements provided in Tabs. 6-10, where we use theoretically calculated β_i from Ref. [48].

Absorbing or emitting a resonant photon of momentum $\hbar k_L$ changes the velocity of an atom by the recoil velocity

$$v_r = \frac{\hbar k_L}{m}. \quad (45)$$

The corresponding change in kinetic energy $\frac{1}{2} m v_r^2 = \frac{\hbar^2 k_L^2}{2m}$ can be written as a recoil energy $E_{\text{rec}} = \hbar \omega_r$, which defines the recoil frequency ω_r

$$E_{\text{rec}} = \hbar \omega_r = \frac{\hbar^2 k_L^2}{2m} \implies \omega_r = \frac{\hbar k_L^2}{2m}. \quad (46)$$

An atom moving at velocity $v \ll c$ sees the optical frequency ω_L shifted by a Doppler shift

$$\Delta\omega_d = \frac{v}{c} \omega_L. \quad (47)$$

In particular, for $v = v_r$ one finds $\Delta\omega_d = 2\omega_r$, showing that a single recoil kick corresponds to a twice as high Doppler shift change.

From these motions arise two key temperatures. The recoil temperature

$$T_r = \frac{\hbar^2 k_L^2}{m k_B} \quad (48)$$

is the temperature corresponding to an ensemble with a one-dimensional root-mean-square momentum of one photon recoil [4]. Note that the single-photon recoil energy E_{rec} (see Eq. 46) can be expressed as a temperature via $k_B T = E_{\text{rec}}$, giving

$$T = \frac{\hbar^2 k_L^2}{2m k_B}, \quad (49)$$

which is exactly half of the rms-defined recoil temperature T_r . The Doppler temperature

$$T_D = \frac{\hbar \Gamma}{2 k_B} \quad (50)$$

is the lowest temperature that Doppler cooling of a two-level atom can reach, set by the balance of Doppler cooling and recoil heating [66]. Since bosonic Sr has no hyperfine or Zeeman substructure in its 1S_0 ground state, sub-Doppler cooling mechanisms are absent for both the $^1S_0 \rightarrow ^1P_1$ and the $^1S_0 \rightarrow ^3P_1$ transitions. Consequently, the minimum achievable temperatures in magneto-optical traps using these transitions are limited by the Doppler cooling limit (see discussion below and Tabs. 6 and 7).

5.4 Magneto-Optical Traps

The magneto-optical trap (MOT) enables laser cooling and confinement of neutral atoms for a wide range of experiments in atomic, molecular, and optical physics. When laser cooling strontium, it is common to start by utilizing the broad $^1S_0 \rightarrow ^1P_1$ “blue” transition at $\lambda \approx 461$ nm. With a natural linewidth on the order of tens of megahertz, this transition provides a large capture velocity, making it ideal for rapidly decelerating thermal atoms and loading them into a MOT [52]. This is crucial, as strontium atoms move at several hundred meters per second after sublimation in an oven that typically operates at temperatures above 400 °C [67]. In practice, however, the $^1S_0 \rightarrow ^1P_1$ transition is not a cycling transition and atoms can decay via the 1D_2 state to the long-lived 3P_2 manifold. To transfer the atoms out of this dark state it is common to repump through 3S_1 , using the $^3P_2 \rightarrow ^3S_1$ transition at $\lambda \approx 707$ nm and the $^3P_0 \rightarrow ^3S_1$ transition at $\lambda \approx 679$ nm [52]. Alternatively, atoms trapped in the metastable $5s5p\ ^3P_2$ state can be repumped via the $5snd\ ^3D_{1,2,3}$, $n \in \{4, 5, 6\}$ manifolds [68, 69].

This returns atoms to the cooling cycle through the $^3P_1 \rightarrow ^1S_0$ decay channel. Using repumping typically increases the number of atoms in the MOT by a factor of 10 – 20, depending on the loading rate [52, 70]. If the repumpers are applied continuously throughout the blue MOT, it maximizes the loading rate, but the number of atoms in the blue MOT will be limited by light-assisted collisions. Without repumping, the atoms that decay to the $m_J = +1, 2$ sublevels of 3P_2 will be magnetically trapped, and the repumpers are only turned on for a few milliseconds toward the end of the blue MOT [71]. This increases the overall number of trapped atoms, but it decreases the loading rate.

Once the atoms are cooled to the millikelvin regime in the blue MOT, they can be transferred into a second-stage “red” MOT operating on the narrow $^1S_0 \rightarrow ^3P_1$ intercombination transition at $\lambda \approx 689$ nm. This transition features a natural linewidth of only a few kHz with an associated Doppler limit of just a few hundred nanokelvin, enabling cooling well below the recoil limit of the blue transition [72]. To improve the transfer of atoms between these two MOT stages, it is common to artificially broaden the linewidth of the red MOT laser [72] and rapidly ramp down the gradient of the magnetic coils [73–75]. The red MOT typically operates with a gradient of 3 – 5 G/cm, whereas the blue MOT operates with a gradient of 30 – 50 G/cm [52, 72]. The broadening of the red MOT laser can be removed once the atoms have been captured from the blue MOT and cooled to the microkelvin regime.

In the red MOT, the scattering force from the radiation pressure becomes comparable to gravity when the red MOT beams are not frequency broadened. Since ^{88}Sr has no hyperfine structure, the atoms in the red MOT will occupy only the surface of an ellipsoid defined by the Zeeman-shifted resonance condition [76]

$$-\hbar \Delta = g_J \mu_B B(\mathbf{r}) , \quad (51)$$

where Δ is the detuning of the MOT laser from the zero-field resonance, g_J is the Landé g -factor, μ_B is the Bohr magneton, $B(\mathbf{r})$ is the magnitude of the quadrupole magnetic field at position \mathbf{r} . Inside this ellipsoidal shell the atoms experience no restoring force, and will accumulate in a thin “cap” at the bottom of the ellipsoid where the upward radiation-pressure force from the MOT beams exactly compensates gravity [77].

In practice, this means that the lowest achievable temperature in the red MOT is set by the requirement to hold atoms against gravity, typically yielding final temperatures on the order of a few hundred nanokelvin [72].

6 Interaction with Electric Fields

The interaction between an atom and an external electric field underpins both static energy shifts and coherent optical manipulations in modern atomic-physics experiments. We first derive the DC Stark effect, separating the induced energy shift into scalar, vector, and tensor contributions based on the atomic polarizability in a static field. These shifts give rise to state-dependent optical dipole potentials and define special operating wavelengths,

the so-called “magic,” “anti-magic,” and “tune-out” wavelengths. Finally, we address the dynamic response of the atom to near-resonant light, deriving the Rabi frequency that governs coherent population oscillations under the rotating-wave approximation.

6.1 Polarizability

In its most general form, the interaction Hamiltonian between an atom and a classical electric field is

$$H_E = -\hat{\mathbf{d}} \cdot \mathbf{E}, \quad (52)$$

where \mathbf{d} is the electric dipole operator and \mathbf{E} is the applied field. We choose the quantization axis along the z -direction, so that for a linearly polarized field is

$$\mathbf{E} = E_z \hat{\mathbf{e}}_z, \quad H_E = -d_z E_z. \quad (53)$$

Far from resonance, the amplitude of the dipole moment is related to the electric field amplitude via [78]

$$d(\mathbf{r}) = \alpha(\omega) E(\mathbf{r}) \quad (54)$$

where $E(\mathbf{r})$ is the local field amplitude. Here

$$\alpha(\omega) = \Re\{\alpha(\omega)\} + i \Im\{\alpha(\omega)\} \quad (55)$$

is the (complex) dynamic polarizability at angular frequency ω . The real part $\Re\{\alpha(\omega)\}$ gives the energy shift, while the imaginary part $\Im\{\alpha(\omega)\}$ accounts for absorption and scattering. Hence, the resulting (time-averaged) energy shift can be written as [79]

$$H_E \approx -\frac{1}{2} \Re\{\alpha(\omega)\} E_z^2. \quad (56)$$

In the following, we define the dynamic polarizability as $\alpha_{\text{tot}} = \Re\{\alpha(\omega)\}$. The dynamic polarizability of a state $|i\rangle$ with angular momentum J_i can be expressed as a sum of contributions from the scalar, vector, and tensor parts [39, 80, 81]

$$\alpha_{\text{tot}}^i(\omega) = \underbrace{\alpha_s^i(\omega)}_{\text{scalar}} + \underbrace{\alpha_v^i(\omega) \sin(2\gamma) \frac{m_{J_i}}{2J_i}}_{\text{vector}} + \underbrace{\alpha_t^i(\omega) \frac{3m_{J_i}^2 - J_i(J_i + 1)}{2J_i(2J_i - 1)} (3\cos^2\beta - 1)}_{\text{tensor}}. \quad (57)$$

where γ is the ellipticity angle of the light polarization and $\cos(\beta)$ is the projection of \mathbf{E} onto the quantization axis. In the generalized form of the polarizability, it is necessary to include the contribution of multiple transitions as well as the frequency of the electric field, ω . The static scalar polarizability of an atomic state $|i\rangle$ is [39]

$$\alpha_s^i = \frac{2}{\hbar} \cdot \frac{1}{3(2J_i + 1)} \sum_k \frac{|\langle k || \mathbf{d} || i \rangle|^2 \omega_{ki}}{\omega_{ki}^2 - \omega^2}, \quad (58)$$

where $\langle k || \mathbf{d} || i \rangle$ is the reduced electric dipole matrix element and $\hbar\omega_{ki} = \hbar\omega_k - \hbar\omega_i$ is the energy difference between the excited state $|k\rangle$ and the initial state $|i\rangle$. The sum runs over all dipole-allowed transitions to states $|k\rangle$. The vector polarizability is given by [39]

$$\alpha_v^i(\omega) = -\frac{2}{\hbar} \sqrt{\frac{6J_i}{(J_i + 1)(2J_i + 1)}} \sum_k (-1)^{J_i + J_k} \begin{Bmatrix} 1 & 1 & 1 \\ J_i & J_k & J_i \end{Bmatrix} \frac{|\langle k || \mathbf{d} || i \rangle|^2 \omega}{\omega_{ki}^2 - \omega^2}, \quad (59)$$

where the curly brackets are the Wigner 6-j symbols. Finally, the tensor polarizability is [39]

$$\alpha_t^i = \frac{2}{\hbar} \sqrt{\frac{10J_i(2J_i - 1)}{3(J_i + 1)(2J_i + 1)(2J_i + 3)}} \sum_k (-1)^{J_i + J_k} \begin{Bmatrix} 1 & 2 & 1 \\ J_i & J_k & J_i \end{Bmatrix} \frac{|\langle k || \mathbf{d} || i \rangle|^2 \omega_{ki}}{(\omega_{ki}^2 - \omega^2)}. \quad (60)$$

The static polarizability can be found by setting $\omega = 0$.

6.2 Types of state-dependent potentials

The optical dipole potential U experienced by an atom in a light field can be written, in the far-off-resonant, low-saturation limit, as [79]

$$U(\mathbf{r}) = -\frac{\alpha_{\text{tot}}^i(\omega)}{\epsilon_0 c} I(\mathbf{r}), \quad (61)$$

where I is the time-averaged intensity. A positive (negative) polarizability produces an attractive (repulsive) potential. At certain “special” wavelengths the polarizabilities of two states satisfy particular relations, giving rise to state-(in)dependent potentials:

- A *magic wavelength* λ_m is defined by

$$\alpha_{\text{tot}}^g(\omega_m) = \alpha_{\text{tot}}^e(\omega_m),$$

so that ground (g) and excited (e) states experience identical potentials. This cancels differential Stark shifts and preserves the unperturbed transition frequency.

- An *anti-magic wavelength* λ_a satisfies

$$\alpha_{\text{tot}}^g(\omega_a) = -\alpha_{\text{tot}}^e(\omega_a),$$

so that the ground- and excited-state dipole potentials have equal magnitude but opposite sign, $U_g(\mathbf{r}) = -U_e(\mathbf{r})$.

- A *tune-out wavelength* λ_t occurs when the polarizability of one state vanishes:

$$\alpha_{\text{tot}}^g(\omega_t^g) = 0 \quad \text{or} \quad \alpha_{\text{tot}}^e(\omega_t^e) = 0.$$

At λ_t , an atom in one internal state experiences no optical potential while in the other it remains confined to a lattice site, enabling state-selective mobility and precise tunneling control.

Theoretical values for the magic, anti-magic, and tune-out wavelengths can be found in databases such as in Refs. [48, 82]. Table 5 presents experimentally measured magic and tune-out wavelengths, supplemented with theoretical values. Note that some values were not measured with the isotope ^{88}Sr and the precise wavelengths could vary due to, e.g., isotope shifts. The tune-out wavelength for the $^1\text{S}_0$ ground state has been measured with high precision [42]. Experimental studies of the $^1\text{S}_0 \rightarrow ^3\text{P}_1(m_J)$ intercombination line have revealed magic wavelengths that produce both attractive, red-detuned optical traps [83–85] and repulsive, blue-detuned traps [86]. Likewise, the $^1\text{S}_0 \rightarrow ^3\text{P}_0$ clock transition supports a blue-detuned magic wavelength at $\sim 389.9\text{ nm}$ [87] and red-detuned magic wavelengths at $\sim 476.8\text{ nm}$ [88], $\sim 497.4\text{ nm}$ [89], and $\sim 813.4\text{ nm}$ [90–92]. Recently, a “triple-magic” condition, where the $^1\text{S}_0$, $^3\text{P}_0$, and $^3\text{P}_2(m_J = 0)$ states experience identical trapping potentials, was demonstrated by tuning the polarization of the red-detuned light to a magic angle β [93]. At $\beta = 90^\circ$, theoretical calculations predict a magic wavelength for the $^3\text{P}_0 \rightarrow ^3\text{P}_2(m_J = 0)$ transition of $\lambda_m = 1010\text{ nm}$ with an uncertainty of $\pm 171\text{ nm}$ [48]. Recent measurements for these states observed a magic condition at $\lambda_m = 914\text{ nm}$ for a polarization angle close to the theoretically predicted angle of $\beta = 79^\circ$, but found no magic condition at $\lambda = 1064\text{ nm}$ [94].

6.3 Calculation of Rabi Frequencies

Consider an atom with a ground-state manifold $|g\rangle = |J_g, m_{J_g}\rangle$ and an excited-state manifold $|e\rangle = |J_e, m_{J_e}\rangle$. A near-resonant laser with an angular frequency ω_L drives the $|g\rangle \leftrightarrow |e\rangle$ transition via the electric-dipole Hamiltonian:

$$H_{\text{int}}(t) = -\hat{\mathbf{d}} \cdot \mathbf{E}(t) \approx -\langle e | \hat{\mathbf{d}} \cdot \hat{\mathbf{e}}_q | g \rangle E_0 \cos(\omega_L t) (|e\rangle \langle g| + |g\rangle \langle e|), \quad (62)$$

where $\langle e | \hat{\mathbf{d}} \cdot \hat{\mathbf{e}}_q | g \rangle$ is the matrix element of the dipole operator between the two levels, including the polarization component. Here, q labels the spherical polarization component. $q = 0$ corresponds to π -polarization, i.e., electric field along the quantization axis, while $q = +1$ and $q = -1$ correspond to right-circular σ^+ and left-circular σ^- polarization, respectively. Under the rotating-wave approximation, the Rabi frequency $\Omega_q^{g \rightarrow e}$ is

$$\Omega_q^{g \rightarrow e} = \frac{1}{\hbar} \langle e | \hat{\mathbf{d}} \cdot \hat{\mathbf{e}}_q | g \rangle E_0. \quad (63)$$

Applying the Wigner–Eckart theorem [78], one can separate the total matrix element into a product of a reduced dipole matrix element $\langle e || \hat{\mathbf{d}} || g \rangle$ (which depends on J_g and J_e but not on m_{J_g} or m_{J_e}) and a Clebsch–Gordan

factor that accounts for the coupling between the specific Zeeman sublevels (m_{J_g}, m_{J_e}) under polarization q . The Clebsch–Gordan coefficient can be calculated using the Wigner 3- j symbol

$$\langle J_g m_{J_g}; 1 q | J_e m_{J_e} \rangle = (-1)^{-J_g+1-m_{J_e}} \sqrt{2J_e+1} \begin{pmatrix} J_g & 1 & J_e \\ m_{J_g} & q & -m_{J_e} \end{pmatrix}. \quad (64)$$

This separation greatly simplifies practical calculations, since all the dependence on magnetic quantum numbers and polarization is contained in the known tabulated Clebsch–Gordan factor. The reduced matrix element of Sr can be found in the literature or in a database [48]. Explicitly, the separation gives [95]

$$\langle e | \hat{\mathbf{d}} \cdot \hat{\mathbf{e}}_q | g \rangle = (-1)^{-J_g+1-m_{J_e}} \begin{pmatrix} J_g & 1 & J_e \\ m_{J_g} & q & -m_{J_e} \end{pmatrix} \langle e || \hat{\mathbf{d}} || g \rangle \equiv w_q^{g \rightarrow e} \langle e || \hat{\mathbf{d}} || g \rangle. \quad (65)$$

Note that here the factor $\sqrt{2J_e+1}$ that appears in the relation between the Clebsch–Gordan coefficients and the Wigner 3- j symbols is absorbed in the definition of the reduced matrix element, see Eq. 44. Substituting into Eq. 63 yields the (real, positive) Rabi frequency

$$\Omega_q^{g \rightarrow e} = |w_q^{g \rightarrow e}| \frac{|\langle e || \hat{\mathbf{d}} || g \rangle|}{\hbar} E_0. \quad (66)$$

We consider an atom driven by a Gaussian laser beam, whose waist is much larger than the spatial extent of the atomic wavefunction. In this case, the atom experiences the peak intensity of the Gaussian beam, given by

$$I_0 = \frac{2P}{\pi w_0^2} = \frac{8P}{\pi D^2}, \quad (67)$$

where P is the total optical power and w_0 is the $1/e^2$ beam radius so that the full $1/e^2$ diameter is $D = 2w_0$. Using Eq. 85, the peak electric-field amplitude is

$$I_0 = \frac{1}{2} c \varepsilon_0 E_0^2 \implies E_0 = \sqrt{\frac{2I_0}{\varepsilon_0 c}} = \sqrt{\frac{16P}{\varepsilon_0 c \pi D^2}}. \quad (68)$$

Using the separated form of the Rabi frequency (see Eq. 66) together with the peak electric-field amplitude (see Eq. 68), we find

$$\Omega_q^{g \rightarrow e} = |w_q^{g \rightarrow e}| \frac{|\langle e || \hat{\mathbf{d}} || g \rangle|}{\hbar} \sqrt{\frac{16P}{\varepsilon_0 c \pi D^2}}. \quad (69)$$

In Tables 6-12, we list numerical values of $\Omega_q^{g \rightarrow e}$ obtained from Eq. 69 under the following common experimental parameters: a laser power of $P = 1$ mW with a Gaussian beam diameter of $D = 1$ mm, and π -polarization ($q = 0$). Specifically, we calculate the Rabi frequency for $m_J = 0 \rightarrow m'_J = 0$ transitions. For the $^3P_1 \rightarrow ^3S_1$ transition, the $m_J = 0 \rightarrow m'_J = 0$ transition is dipole-forbidden. Instead, we evaluate the Rabi frequency for the allowed σ^+ transition $m_{J_g} = 0 \rightarrow m_{J_e} = +1$ ($q = +1$).

We now discuss the calculation of the Rabi frequency on the $^1S_0 \rightarrow ^3P_0$ clock transition. In Eq. 26, we discussed the mixing of the 3P_0 state with the 3P_1 state. The resulting induced transition rate, i.e., the on-resonance Rabi frequency, is [26]

$$\Omega_{\text{clock}} = \frac{1}{\hbar^2 \Delta_{10}} \langle ^1S_0 | \hat{\mathbf{d}} \cdot \mathbf{E} | ^3P_1 \rangle \langle ^3P_1 | \hat{\boldsymbol{\mu}} \cdot \mathbf{B} | ^3P_0 \rangle \propto |\mathbf{B}| \sqrt{I_{\text{clock}}}. \quad (70)$$

where I_{clock} is the clock-laser intensity. The clock Rabi frequency can be derived to be [27]

$$\Omega_{\text{clock}}(B) = \frac{\mu_C B}{\hbar \Delta_{10}} \sqrt{\frac{3\Gamma_{3P1} \lambda^3 I_{\text{clock}}}{4\pi^2 \hbar c}} (\hat{\mathbf{e}} \cdot \mathbf{B}), \quad (71)$$

where λ is the clock transition wavelength, $\hat{\mathbf{e}} \cdot \mathbf{B}$ is the projection of the clock beam polarization onto the magnetic field axis, and μ_C and Δ_{10} as defined previously. The constant terms can be combined in a single value $\alpha = 2\pi \times 201.9(2) \frac{\text{Hz}}{\text{T} \sqrt{(\text{mW}/\text{cm}^2)}}$ [26]. Then, the Rabi frequency is given by

$$\Omega_{\text{clock}} = \alpha \sqrt{I_{\text{clock}}} |\mathbf{B}| \cos \theta, \quad (72)$$

where θ is the angle between the clock-laser polarization and the magnetic field.

The beam that excites the clock transition also couples to other transitions and hence induces an AC Stark shift on both the ground state $|^1S_0\rangle$ and the clock state $|^3P_0\rangle$. Since both states have total angular momentum $J = 0$, their dynamic polarizabilities are purely scalar, and hence the induced shift is independent of the probe polarization. The differential light shift of the clock transition is therefore simply proportional to the intensity of the clock beam

$$\Delta\omega_I(I_{\text{clock}}) = \kappa I_{\text{clock}}. \quad (73)$$

where $\kappa = -2\pi \times 18 \text{ mHz}/(\text{mW}/\text{cm}^2)$ [26, 27]. Because the Rabi frequency scales as $\Omega_{\text{clock}} \propto \sqrt{I_{\text{clock}}}$ (cf. Eq. 70), the relative light shift per Rabi oscillation grows as

$$\frac{\Delta\omega_I}{\Omega} \propto \frac{I}{\sqrt{I}} = \sqrt{I}. \quad (74)$$

In practice, this means that pushing to higher clock Rabi frequencies by increasing the clock beam intensities inevitably amplifies the differential light shift faster than it improves the Rabi rate. Thus, higher clock beam intensities demand correspondingly better intensity stabilization to keep $\Delta\omega_I$ under control. Since the clock states have $J = 0$, there is no first-order Zeeman shift of the $^1S_0 \rightarrow ^3P_0$ transition. To second order in the magnetic-dipole perturbation one finds [26, 27]

$$\Delta\omega_B(\mathbf{B}) = -\frac{\mu_C^2}{\Delta_{10}} \mathbf{B}^2 \equiv \eta \mathbf{B}^2, \quad (75)$$

where $\eta \approx -2\pi \times 0.23 \text{ Hz}/\text{G}^2$ [27]. This quadratic Zeeman shift is one of the dominant systematics in bosonic Sr clocks [96]. Its magnitude scales as \mathbf{B}^2 , so operating at lower bias fields (at the expense of reduced Rabi rate $\Omega \propto |\mathbf{B}|$) can mitigate Zeeman-induced inaccuracy.

At sufficiently high magnetic fields, mixing of the 3P_2 state also gives the $^1S_0 \rightarrow ^3P_2$ transition an electric dipole character similar to the clock transition. However, in contrast to the clock transition, the $^1S_0 \rightarrow ^3P_2$ transition can be driven even without magnetic field, because it is magnetic-quadrupole (M2) allowed [39]. The corresponding Rabi frequency depends on the laser's magnetic-field amplitude (i.e., beam intensity), its propagation direction relative to the quantization axis, and the light's polarization. Note that in the case of M2 transitions, magnetic quadrupole selection rules apply instead of the standard dipole selection rules. A full derivation of the M2 Rabi frequency is beyond the scope of this review. Instead, we adopt in Tab. 12 the experimentally measured value from Ref. [61] and refer the reader to Ref. [39] for further details.

7 Resonance Fluorescence

In this section, we analyze the interaction of a two-level atom with a monochromatic classical electromagnetic field. Under the electric-dipole and rotating-wave approximations, the atom behaves as an ideal two-level system whose dynamics are governed by the optical Bloch equations. We derive these equations, solve for the steady-state excited-state population, and then obtain expressions for the total photon scattering rate, the saturation intensity, and the on-resonance scattering cross section. Finally, we show how to determine the Rabi frequency from the power and geometry of a laser beam, combined with the relevant atomic dipole matrix element and angular-momentum coupling factors.

7.1 Optical Bloch Equations

Consider an atom with ground state $|g\rangle$ and excited state $|e\rangle$, separated by an energy $\hbar\omega_0$. We drive the $|g\rangle \leftrightarrow |e\rangle$ transition with a classical, linearly polarized, monochromatic field of the form

$$\mathbf{E}(t) = E_0 \hat{\mathbf{e}} \cos(\omega_L t), \quad (76)$$

where E_0 is the real field amplitude, $\hat{\mathbf{e}}$ is the unit polarization vector, and ω_L is the laser frequency. The atom-field interaction Hamiltonian in the electric-dipole approximation is

$$H_{\text{int}} = -\hat{\mathbf{d}} \cdot \mathbf{E}(t) = -(d \hat{\sigma}_+ + d^* \hat{\sigma}_-) E_0 \cos(\omega_L t), \quad (77)$$

where $\hat{\mathbf{d}}$ is the atomic dipole moment, $d = \langle e | \hat{\mathbf{d}} \cdot \hat{\mathbf{e}} | g \rangle$ is the (complex) dipole matrix element, and $\hat{\sigma}_- = |g\rangle\langle e|$ (with $\hat{\sigma}_+ = \hat{\sigma}_-^\dagger$) is the lowering operator for the two-level system. We define the Rabi frequency as

$$\Omega = \frac{d E_0}{\hbar}. \quad (78)$$

We move into a frame rotating at the laser frequency ω_L and apply the rotating-wave approximation (RWA). Then, the density operator ρ of the two-level atom is described by the optical Bloch equations [4]

$$\dot{\rho}_{gg} = \frac{i\Omega}{2}(\rho_{eg} - \rho_{ge}) + \Gamma \rho_{ee}, \quad (79a)$$

$$\dot{\rho}_{ee} = -\frac{i\Omega}{2}(\rho_{eg} - \rho_{ge}) - \Gamma \rho_{ee}, \quad (79b)$$

$$\dot{\rho}_{ge} = -(\gamma + i\Delta) \rho_{ge} - \frac{i\Omega}{2}(\rho_{ee} - \rho_{gg}), \quad (79c)$$

where $\rho_{ij} = \langle i|\rho|j\rangle$ are the matrix elements of the density operator in the $\{|g\rangle, |e\rangle\}$ basis, $\gamma = \frac{\Gamma}{2} + \gamma_c$ is the total coherence-decay (“transverse”) rate, with γ_c a pure-dephasing rate (e.g., due to collisions), and $\Delta = \omega_L - \omega_0$ is the detuning of the driving field from atomic resonance.

In writing Eqs. 79, we have neglected any additional couplings to auxiliary levels or motional effects. The term $\Gamma \rho_{ee}$ in the population equations accounts for radiative decay from $|e\rangle$ to $|g\rangle$, while the coherence ρ_{ge} and its conjugate $\rho_{eg} = \rho_{ge}^*$ evolve under both dephasing and the coherent drive Ω .

7.2 Steady-State Excited-State Population

Here, we are primarily interested in the long-time (steady-state) solution, where $\dot{\rho}_{ij} = 0$ for all i, j . In the steady state and assuming the purely radiative case ($\gamma = \Gamma/2$, i.e., $\gamma_c = 0$), one finds

$$\rho_{ee}^{(\infty)} = \frac{\left(\frac{\Omega}{\Gamma}\right)^2}{1 + 4\left(\frac{\Delta}{\Gamma}\right)^2 + 2\left(\frac{\Omega}{\Gamma}\right)^2}. \quad (80)$$

We can rewrite this equation

$$\rho_{ee}^{(\infty)} = \frac{s/2}{1 + s + 4(\Delta/\Gamma)^2}, \quad (81)$$

where s is the on-resonance saturation parameter, given by

$$s = \frac{2\Omega^2}{\Gamma^2}. \quad (82)$$

Equation 80 shows that, on resonance ($\Delta = 0$), the excited-state population saturates to $1/2$ when $\Omega \gg \Gamma$.

7.3 Total Photon Scattering Rate

The total photon scattering (or fluorescence) rate is the rate at which population decays from the excited state, given by

$$R_{sc} = \Gamma \rho_{ee}. \quad (83)$$

In the steady state, we find

$$R_{sc} = \Gamma \rho_{ee}^{(\infty)} = \frac{\Gamma}{2} \frac{s}{1 + s + 4(\Delta/\Gamma)^2}, \quad (84)$$

where we have set $s = 2\Omega^2/\Gamma^2$ as above. Rewriting Eq. 84 in terms of the incident intensity I leads naturally to the definition of the saturation intensity I_{sat} .

7.4 Saturation Intensity

The average intensity of a plane electromagnetic wave in free space is

$$I = \frac{1}{2} c \varepsilon_0 E_0^2, \quad (85)$$

where c is the speed of light and ε_0 is the vacuum permittivity. In terms of the Rabi frequency (see Eq. 78), one finds

$$I = \frac{1}{2} c \varepsilon_0 \left(\hbar \frac{\Omega}{|d|} \right)^2 = \frac{c \varepsilon_0 \hbar^2}{2|d|^2} \Omega^2. \quad (86)$$

We define the (on-resonance) saturation intensity I_{sat} using the condition that $s = 1$ when $I = I_{\text{sat}}$. Since $s = 2\Omega^2/\Gamma^2$, setting $s = 1$ yields

$$I_{\text{sat}} = \frac{c\epsilon_0 \hbar^2}{2|d|^2} \frac{\Gamma^2}{2} = \frac{c\epsilon_0 \hbar^2 \Gamma^2}{4|d|^2}. \quad (87)$$

Using Eq. 43, we find the saturation intensity for a cycling transition

$$I_{\text{sat}} = \frac{\hbar \omega_0^3 \Gamma}{12\pi c^2} = \frac{\pi \hbar c \Gamma}{3\lambda^3}. \quad (88)$$

Equivalently, I_{sat} and Ω are often defined as

$$\frac{I}{I_{\text{sat}}} = \frac{2\Omega^2}{\Gamma^2} = s \implies \Omega = \frac{\Gamma}{\sqrt{2}} \sqrt{\frac{I}{I_{\text{sat}}}}. \quad (89)$$

Using this definition of I_{sat} , we can write the scattering rate (see Eq. 84) as

$$R_{\text{sc}} = \left(\frac{\Gamma}{2}\right) \frac{\left(\frac{I}{I_{\text{sat}}}\right)}{1 + 4\left(\frac{\Delta}{\Gamma}\right)^2 + \left(\frac{I}{I_{\text{sat}}}\right)}. \quad (90)$$

When the laser is exactly on resonance ($\Delta = 0$), the scattering rate reduces to

$$R_{\text{sc}}(\Delta = 0) = \frac{\Gamma}{2} \frac{I/I_{\text{sat}}}{1 + I/I_{\text{sat}}}. \quad (91)$$

Thus, on resonance, the scattering rate on a fully saturated transition ($I \gg I_{\text{sat}}$) approaches $\Gamma/2$, consistent with the fact that at saturation $\rho_{ee}^{(\infty)} \rightarrow 1/2$.

7.5 On-Resonance Scattering Cross Section

It is often convenient to express the scattering properties in terms of an effective cross section $\sigma(\Delta, I)$, defined as the power radiated by the atom divided by the incident energy flux so that the power scattered by the atom is $\sigma(\Delta, I) I$. Using Eq. 90, we can calculate the scattering cross section as

$$R_{\text{sc}} = \sigma(\Delta, I) I \implies \sigma(\Delta, I) = \frac{R_{\text{sc}}}{I} = \frac{\Gamma}{2I} \frac{I/I_{\text{sat}}}{1 + I/I_{\text{sat}} + 4(\Delta/\Gamma)^2}. \quad (92)$$

We define the low-intensity on-resonance cross section as

$$\sigma_0 = \frac{\hbar \omega_0 \Gamma}{2 I_{\text{sat}}}. \quad (93)$$

For a cycling transition, this reduces to [97]

$$\sigma_0 = \frac{3\lambda^2}{2\pi}. \quad (94)$$

Then, we can write the scattering cross section as

$$\sigma(\Delta, I) = \frac{\sigma_0}{1 + 4(\Delta/\Gamma)^2 + I/I_{\text{sat}}}. \quad (95)$$

On resonance ($\Delta = 0$), this reduces to

$$\sigma(0, I) = \frac{\sigma_0}{1 + I/I_{\text{sat}}}, \quad (96)$$

showing that at $I = I_{\text{sat}}$ the scattering cross section is half of its low-intensity value σ_0 .

8 Data Tables

Table 1: Fundamental Physical Constants (2022 CODATA recommended values) [8].

Constant	Symbol	Value
Speed of Light	c	$2.997\,924\,58 \times 10^8 \text{ m/s (exact)}$
Permeability of Vacuum	μ_0	$1.256\,637\,061\,27(20) \times 10^{-6} \text{ N/A}^2$
Permittivity of Vacuum	ε_0	$(\mu_0 c^2)^{-1} \approx 8.854\,187\,818\,8(14) \times 10^{-12} \text{ F/m}$
Planck's Constant	h	$6.626\,070\,15 \times 10^{-34} \text{ J s (exact)}$
Reduced Planck Constant	\hbar	$\sim 1.054\,571\,817 \times 10^{-34} \text{ J s}$
Elementary Charge	e	$1.602\,176\,634 \times 10^{-19} \text{ C (exact)}$
Bohr Magneton	μ_B	$9.274\,010\,065\,7(29) \times 10^{-24} \text{ J/T}$
Atomic Mass Unit	u	$1.660\,539\,068\,92(52) \times 10^{-27} \text{ kg}$
Electron Mass	m_e	$9.109\,383\,713\,9(28) \times 10^{-31} \text{ kg}$
Bohr Radius	a_0	$5.291\,772\,105\,44(82) \times 10^{-11} \text{ m}$
Boltzmann Constant	k_B	$1.380\,649 \times 10^{-23} \text{ J/K (exact)}$

Table 2: Physical properties of strontium-88.

Property	Symbol	Value	Reference
Atomic Number	Z	38	
Total Nucleons	$Z + N$	88	
Nuclear Spin	I	0	
Particle Statistics		bosonic	
Relative Natural Abundance	$\eta (^{88}\text{Sr})$	82.58(1)%	[7]
Nuclear Lifetime	τ_n	stable	
Atomic Mass	m	87.905 612 254(6) u $1.459\,707\,035\,3(5) \times 10^{-25} \text{ kg}$	[9]
RMS Nuclear Charge Radius	R	4.2240(18) fm	[98]
Electron Spin g-Factor	g_S	2.002 319 304 360 92(36)	[8]
Electron Orbital g-Factor	g_L	$\sim 0.999\,993\,76$	
Density at 20 °C	ρ_m	2582(4) kg/m ³	[12]
Molar Volume at 20 °C	V_m	33.94(5) cm ³ /mol	[12]
Melting Point	T_M	1050 K (777 °C)	[7]
Boiling Point	T_B	1655 K (1382 °C)	[7]
Specific Heat Capacity	c_p	0.306 J/(g K)	[7]
Molar Heat Capacity	C_p	26.79 J/(mol K)	[7]
Vapor Pressure at 25 °C	P	$3.39(17) \times 10^{-18} \text{ Pa}$ $2.54(13) \times 10^{-20} \text{ Torr}$	[13]
Ionization Limit	E_I	45 932.09(15) cm ⁻¹ 5.694 853(19) eV	[99]

Table 3: Scattering lengths between the strontium isotopes, given in units of a_0 .

	^{84}Sr	^{86}Sr	^{87}Sr	^{88}Sr
^{84}Sr	122.7(3) [100–102]	31.9(3) [100–102]	−56.1(10) [100–102]	1768(124) [100, 102]
^{86}Sr		811(22) ($R_B : 2.0$) [100–104]	162.5(5) [100–102]	97.40(10) [100–102, 104]
^{87}Sr			96.20(10) [100–102]	54.98(19) [100–102]
^{88}Sr				−0.8(18) ($R_B : 3.1$) [47, 100–104]

Table 4: Landé g_J factors and Zeeman coefficients $\mu_B g_J$ for selected states of ^{88}Sr .

State	g_J	$\mu_B g_J$ (MHz/G)
$^1\text{S}_0$	0	0
$^1\text{P}_1$	1	1.39962
$^3\text{P}_0$	0	0
$^3\text{P}_1$	1.50116	2.10106
$^3\text{P}_2$	1.50116	2.10106
$^3\text{S}_1$	2.00232	2.80249

Table 5: Experimentally measured magic and tune-out wavelengths, supplemented with theoretical polarizability values.

Type	Transition	β (°)	λ (nm)	$\omega_0/2\pi$ (THz)	α_{tot} (a.u.)
magic	$^1\text{S}_0 - ^3\text{P}_0$	$\forall \angle$	389.889(9) [87]	768.92(2)	−459 [105]
		$\forall \angle$	476.82362(8) [88]	628.7282(1) [88]	2818 [48]
		$\forall \angle$	497.4363(3) [89]	602.67507(36)	1337 [48]
	$^1\text{S}_0 - ^3\text{P}_0 - ^3\text{P}_2 (m_J = 0)$	78.49(3) [93]	813.427 373(96)	368.554 67(4) [90–92]	286 [48]
	$^1\text{S}_0 - ^3\text{P}_1 (m_J = 0)$	0	473.371(6) [85]	633.314(8)	3573(16) [85]
		24(1) [84]	~ 515.13 [84]	~ 581.97	949 [48]
		90	914(1) [83]	328.0(4)	261 [48]
	$^1\text{S}_0 - ^3\text{P}_1 (m_J = 1)$	0	435.827(25) [86]	687.87(4)	−1558(57) [86]
		0	473.117(15) [85]	633.65(2)	3637(17) [85]
	$^3\text{P}_0 - ^3\text{P}_2 (m_J = 0)$	~ 9.5 [106]	~ 539.91 [106]	~ 555.26	431 [48]
tune-out	$^1\text{S}_0$	$\forall \angle$	689.222 22(2)	434.972 130(10) [42]	0

Table 6: $^1S_0 \rightarrow ^1P_1$ Transition (Blue MOT).

Parameter	Symbol	Value	Ref.
Frequency	ω_0	$2\pi \times 650.503\,47(28)$ THz	
Transition Energy	$\hbar\omega_0$	2.690 266 2(12) eV	
Wavelength (vacuum)	λ	460.8622(2) nm	[33, 107]
Wavelength (air)	λ_{air}	460.7377(2) nm	
Wavenumber (vacuum)	$k_L/2\pi$	21 698.460(9) cm^{-1}	
Lifetime excited state	τ	5.255(12) ns R_B : 3.5	[42–47]
Decay rate	Γ	$190.3(4) \times 10^6 \text{ s}^{-1}$	
Natural Line Width	$\Delta\nu_{\text{FWHM}}$	$2\pi \times 30.29(7)$ MHz	
Branching Ratio	β	0.999 949 48(96)	[48]
Oscillator strength	f	1.818(4)	
Recoil velocity	v_r	~ 9.8496 mm/s	
Recoil energy	ω_r	$\sim 2\pi \times 10.686$ kHz	
Recoil temperature	T_r	~ 1026 nK	
Doppler shift ($v = v_r$)	$\Delta\omega_d$	$\sim 2\pi \times 21.372$ kHz	
Doppler Temperature	T_D	727(2) μK	
Reduced E1 Matrix Element	$\langle J er J' \rangle$	5.252(6) ea_0	
Saturation Intensity	I_{sat}	40.44(9) mW/cm^2	
Resonant Cross Section	σ_0	$\sim 1.0141 \times 10^{-13} \text{ m}^2$	
Rabi Frequency $P = 1 \text{ mW}$, $D = 1 \text{ mm}$	$\Omega_0^{ m_J=0\rangle \rightarrow m'_J=0\rangle}$	$2\pi \times 53.74(6)$ MHz	
Isotope Shifts	$\nu(^{84}\text{Sr}) - \nu(^{88}\text{Sr})$ $\nu(^{86}\text{Sr}) - \nu(^{88}\text{Sr})$ $\nu(^{87}\text{Sr}) - \nu(^{88}\text{Sr})$	$-275(3)$ MHz (R_B : 12.5) $-126(2)$ MHz (R_B : 10.7) $-47(2)$ MHz (R_B : 7.2)	[108, 109]

Table 7: $^1S_0 \rightarrow ^3P_1$ Intercombination Transition (Red MOT).

Parameter	Symbol	Value	Ref.
Frequency	ω_0	$2\pi \times 434.829\,121\,309(9)$ THz	[34, 110]
Transition Energy	$\hbar\omega_0$	1.798 308 750 68(4) eV	
Wavelength (vacuum)	λ	689.448 896 839(14) nm	
Wavelength (air)	λ_{air}	689.265 521(7) nm	
Wavenumber (vacuum)	$k_L/2\pi$	14 504.338 241 5(3) cm^{-1}	
Lifetime excited state	τ	21.28(4) μs R_B : 1.4	[50, 54–57]
Decay rate	Γ	$47.00(9) \times 10^3 \text{ s}^{-1}$	
Natural Line Width	$\Delta\nu_{\text{FWHM}}$	$2\pi \times 7.481(15)$ kHz	
Oscillator strength	f	0.001 005(2)	
Recoil velocity	v_r	~ 6.584 mm/s	
Recoil energy	ω_r	$\sim 2\pi \times 4.775$ kHz	
Recoil temperature	T_r	~ 458 nK	
Doppler shift ($v = v_r$)	$\Delta\omega_d$	$\sim 2\pi \times 9.5496$ kHz	
Doppler Temperature	T_D	179.5(4) nK	
Reduced E1 Matrix Element	$\langle J er J' \rangle$	0.151 02(15) ea_0	
Saturation Intensity	I_{sat}	2.983(6) $\mu\text{W}/\text{cm}^2$	
Resonant Cross Section	σ_0	$\sim 2.2696 \times 10^{-13} \text{ m}^2$	
Rabi Frequency $P = 1 \text{ mW}$, $D = 1 \text{ mm}$	$\Omega_0^{ m_J=0\rangle \rightarrow m'_J=0\rangle}$	$2\pi \times 1.5454(15)$ MHz	
Isotope shifts	$\nu(^{84}\text{Sr}) - \nu(^{88}\text{Sr})$	−351.496(5) MHz	[111]
	$\nu(^{86}\text{Sr}) - \nu(^{88}\text{Sr})$	−163.8174(2) MHz	[110, 111]
	$\nu(^{87}\text{Sr}) - \nu(^{88}\text{Sr})$	−62.186(12) MHz	[34, 111]

Table 8: $^3P_0 \rightarrow ^3S_1$ Repump Transition (679 nm).

Parameter	Symbol	Value	Ref.
Frequency	ω_0	$2\pi \times 441.332\,751\,3(7)$ THz	[34]
Transition Energy	$\hbar\omega_0$	1.825 205 603(3) eV	
Wavelength (vacuum)	λ	679.288 943(1) nm	
Wavelength (air)	λ_{air}	679.108 203(7) nm	
Wavenumber (vacuum)	$k_L/2\pi$	14 721.275 99(2) cm^{-1}	
Lifetime excited state	τ	13.89(21) ns R_B : 1.9	[42, 58–60]
Decay rate	Γ	$72.0(11) \times 10^6 \text{ s}^{-1}$	
Natural Line Width	$\Delta\nu_{\text{FWHM}}$	$2\pi \times 11.46(17)$ MHz	
Branching Ratio	β	0.1161(10)	[48]
Partial decay rate	Γ_{partial}	$8.36(14) \times 10^6 \text{ s}^{-1}$	
Recoil velocity	v_r	~ 6.682 mm/s	
Recoil energy	ω_r	$\sim 2\pi \times 4.919$ kHz	
Recoil temperature	T_r	~ 472 nK	
Doppler shift ($v = v_r$)	$\Delta\omega_d$	$\sim 2\pi \times 9.837$ kHz	
Reduced E1 Matrix Element	$\langle J er J' \rangle$	1.970(17) ea_0	
Rabi Frequency $P = 1 \text{ mW}$, $D = 1 \text{ mm}$	$\Omega_0^{ m_J=0\rangle \rightarrow m'_J=0\rangle}$	$2\pi \times 20.16(17)$ MHz	
Isotope shift	$\nu(^{87}\text{Sr}) - \nu(^{88}\text{Sr})$	7.29(30) MHz	[34, 35, 111, 112]

Table 9: $^3P_1 \rightarrow ^3S_1$ Transition (688 nm).

Parameter	Symbol	Value	Ref.
Frequency	ω_0	$2\pi \times 435.731\,697\,2(5)$ THz	[34]
Transition Energy	$\hbar\omega_0$	1.802 041 505(2) eV	
Wavelength (vacuum)	λ	688.020 770 4(8) nm	
Wavelength (air)	λ_{air}	687.837 765(7) nm	
Wavenumber (vacuum)	$k_L/2\pi$	14 534.444 933(17) cm^{-1}	
Lifetime excited state	τ	13.89(21) ns R_B : 1.9	[42, 58–60]
Decay rate	Γ	$72.0(11) \times 10^6 \text{ s}^{-1}$	
Natural Line Width	$\Delta\nu_{\text{FWHM}}$	$2\pi \times 11.46(17)$ MHz	
Branching Ratio	β	0.3405(24)	[48]
Partial decay rate	Γ_{partial}	$24.5(4) \times 10^6 \text{ s}^{-1}$	
Recoil velocity	v_r	~ 6.598 mm/s	
Recoil energy	ω_r	$\sim 2\pi \times 4.795$ kHz	
Recoil temperature	T_r	~ 460 nK	
Doppler shift ($v = v_r$)	$\Delta\omega_d$	$\sim 2\pi \times 9.589$ kHz	
Reduced E1 Matrix Element	$\langle J er J' \rangle$	3.439(29) ea_0	
Rabi Frequency $P = 1$ mW, $D = 1$ mm	$\Omega_1^{ m_J=0\rangle \rightarrow m'_J=1\rangle}$	$2\pi \times 24.88(21)$ MHz	
Isotope shift	$\nu(^{87}\text{Sr}) - \nu(^{88}\text{Sr})$	7.29(30) MHz	[34, 111]

Table 10: $^3P_2 \rightarrow ^3S_1$ Repump Transition (707 nm).

Parameter	Symbol	Value	Ref.
Frequency	ω_0	$2\pi \times 423.916\,34(3)$ THz	[40]
Transition Energy	$\hbar\omega_0$	1.753 177 13(12) eV	
Wavelength (vacuum)	λ	707.197 21(5) nm	
Wavelength (air)	λ_{air}	707.009 23(5) nm	
Wavenumber (vacuum)	$k_L/2\pi$	14 140.3272(10) cm^{-1}	
Lifetime excited state	τ	13.89(21) ns R_B : 1.9	[42, 58–60]
Decay rate	Γ	$72.0(11) \times 10^6 \text{ s}^{-1}$	
Natural Line Width	$\Delta\nu_{\text{FWHM}}$	$2\pi \times 11.46(17)$ MHz	
Branching Ratio	β	0.5432(25)	[48]
Partial decay rate	Γ_{partial}	$39.1(6) \times 10^6 \text{ s}^{-1}$	
Recoil velocity	v_r	~ 6.419 mm/s	
Recoil energy	ω_r	$\sim 2\pi \times 4.538$ kHz	
Recoil temperature	T_r	~ 436 nK	
Doppler shift ($v = v_r$)	$\Delta\omega_d$	$\sim 2\pi \times 9.076$ kHz	
Reduced E1 Matrix Element	$\langle J er J' \rangle$	4.526(36) ea_0	
Rabi Frequency $P = 1$ mW, $D = 1$ mm	$\Omega_0^{ m_J=0\rangle \rightarrow m'_J=0\rangle}$	$2\pi \times 29.29(23)$ MHz	
Isotope shift	$\nu(^{87}\text{Sr}) - \nu(^{88}\text{Sr})$	8.0(3) MHz	[34, 39]

Table 11: $^1S_0 \rightarrow ^3P_0$ Clock Transition (698 nm).

Parameter	Symbol	Value	Ref.
Frequency	ω_0	$2\pi \times 429.228\,066\,418\,007\,01(9)$ THz	[37]
Transition Energy	$\hbar\omega_0$	1.775 144 648 898 040 2(4) eV	
Wavelength (vacuum)	λ	698.445 608 419 382 44(14) nm	[37]
Wavelength (air)	λ_{air}	698.259 898(7) nm	
Wavenumber (vacuum)	$k_L/2\pi$	14 317.507 160 837 482(3) cm^{-1}	
Recoil velocity	v_r	~ 6.499 mm/s	
Recoil energy	ω_r	$\sim 2\pi \times 4.653$ kHz	
Recoil temperature	T_r	~ 447 nK	
Doppler shift ($v = v_r$)	$\Delta\omega_d$	$\sim 2\pi \times 9.305$ kHz	
Rabi Frequency $P = 1$ mW, $D = 1$ mm, $B = 500$ G	Ω_0	$2\pi \times 161.2(2)$ Hz	
Isotope shifts	$\nu(^{84}\text{Sr}) - \nu(^{88}\text{Sr})$	$-349.656(10)$ MHz	[111]
	$\nu(^{86}\text{Sr}) - \nu(^{88}\text{Sr})$	$-162.939(11)$ MHz	[111]
	$\nu(^{87}\text{Sr}) - \nu(^{88}\text{Sr})$	$-62.188\,134\,004(10)$ MHz	[34, 35, 111, 112]

Table 12: $^1S_0 \rightarrow ^3P_2$ M2 Transition (671 nm).

Parameter	Symbol	Value	Ref.
Frequency	ω_0	$2\pi \times 446.647\,242\,704(2)$ THz	[39]
Transition Energy	$\hbar\omega_0$	1.847 184 573 571(8) eV	
Wavelength (vacuum)	λ	671.206 333 179(3) nm	
Wavelength (air)	λ_{air}	671.027 689(7) nm	
Wavenumber (vacuum)	$k_L/2\pi$	14 898.548 338 53(7) cm^{-1}	
Lifetime excited state	τ	520(310) s	[63]
Decay rate	Γ	$1.9(11) \times 10^{-3} \text{ s}^{-1}$	
Natural Line Width	$\Delta\nu_{\text{FWHM}}$	$2\pi \times 0.3(2)$ mHz	
Branching ratio	β	0.08(5)	
Partial decay rate	Γ_{partial}	$152(43) \times 10^{-6} \text{ s}^{-1}$	[61]
Recoil velocity	v_r	~ 6.763 mm/s	
Recoil energy	ω_r	$\sim 2\pi \times 5.038$ kHz	
Recoil temperature	T_r	~ 484 nK	
Doppler shift ($v = v_r$)	$\Delta\omega_d$	$\sim 2\pi \times 10.076$ kHz	
M2 Matrix Element	$\langle ^1S_0 M2 ^3P_2 \rangle$	22.6(4) μ_B	[61]
Rabi Frequency $P = 1$ mW, $D = 1$ mm, $\theta = 14(2)^\circ$	$\Omega_{\pm 1}^{m_J=0 \rightarrow m'_J=0}$	$2\pi \times 189(1)$ MHz	[61]
Isotope shift	$\nu(^{87}\text{Sr}) - \nu(^{88}\text{Sr})$	$-62.91(4)$ MHz	[39]

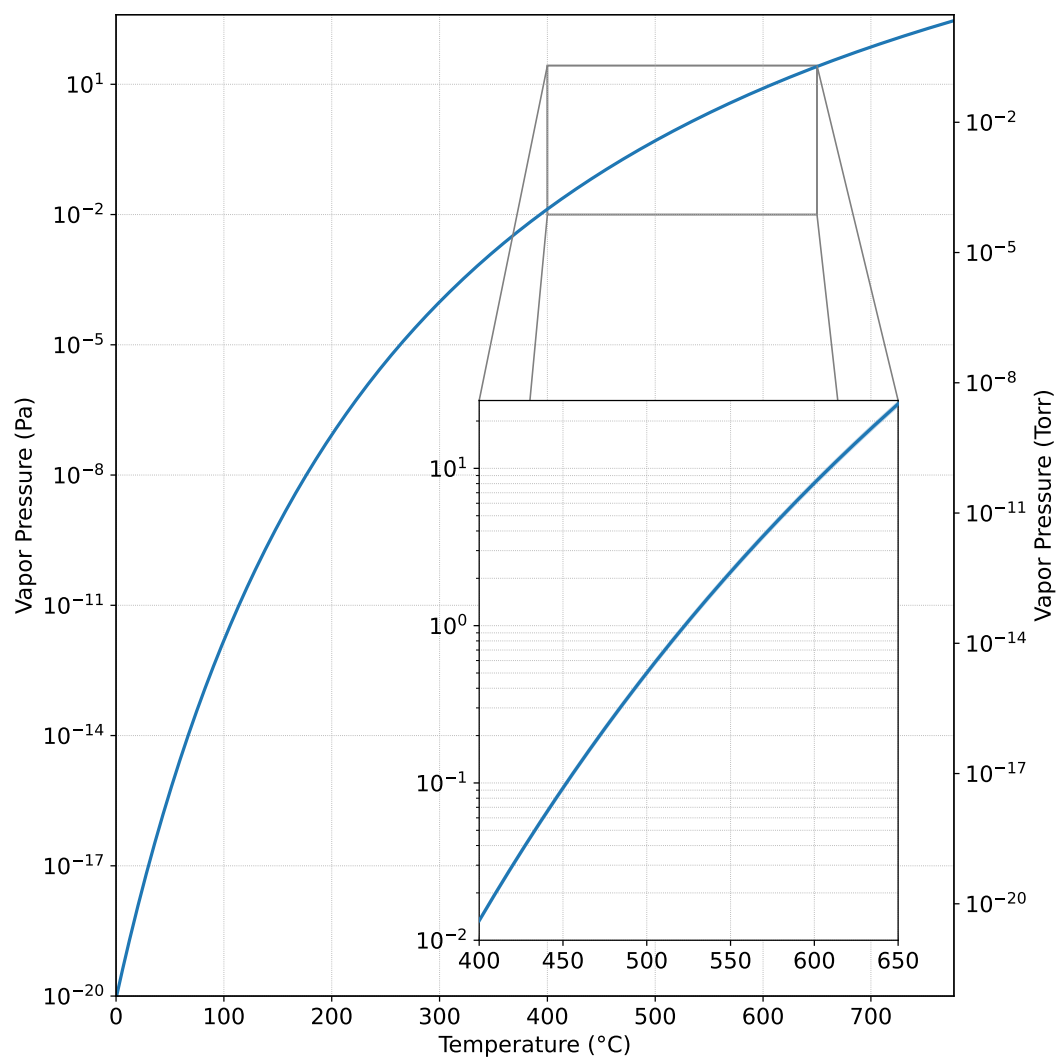


Figure 1: Vapor pressure of strontium as a function of temperature, calculated using Eq. 7.

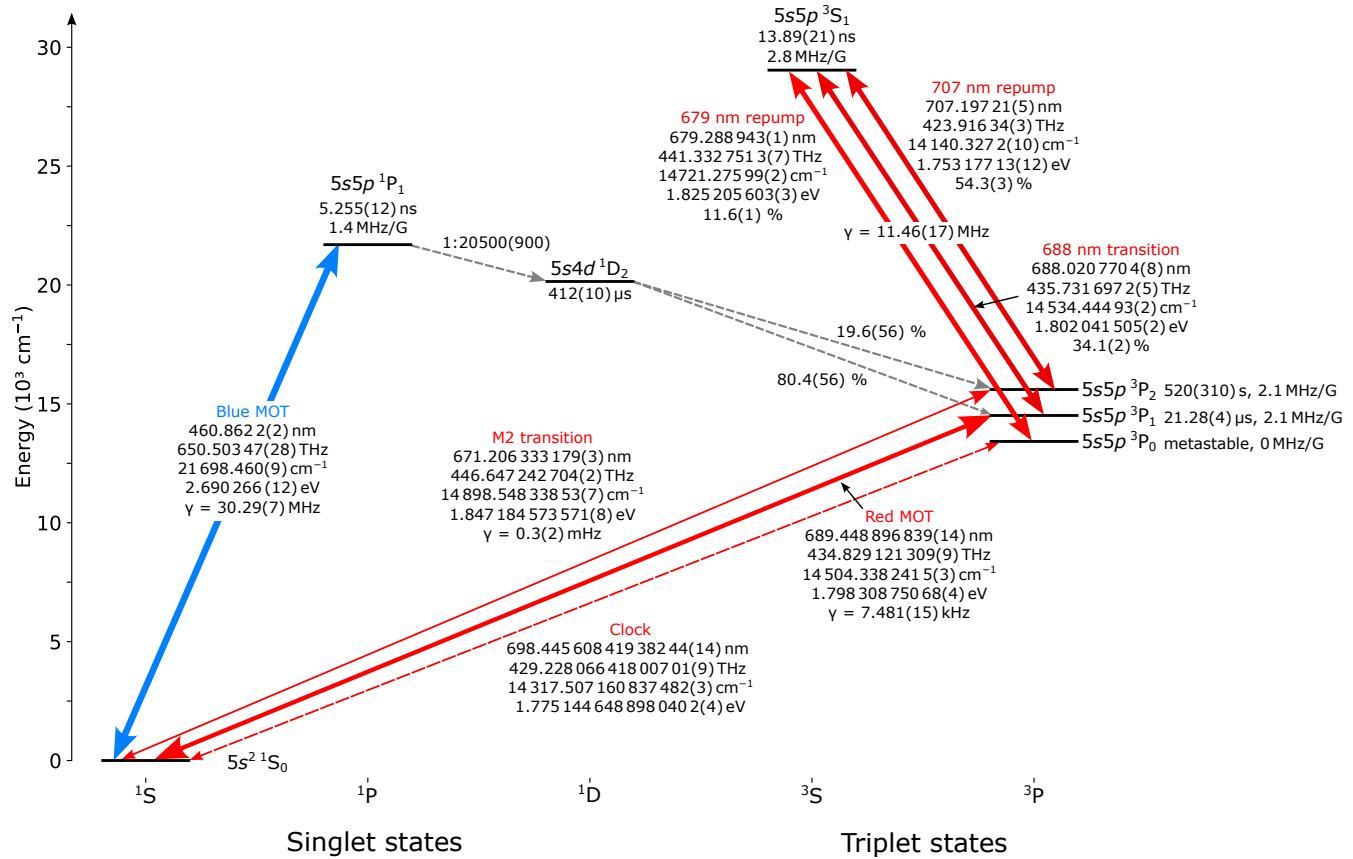


Figure 2: Data of the transitions discussed in this reference. Tables 6-12 list the frequencies, wavelengths, energies, linewidths, and branching ratios of the transitions as well as the lifetime of the states with the corresponding references. The Zeeman splittings between adjacent magnetic sublevels can be found in Tab. 4. Note that for clarity the 3P_0 state has been shifted downward and the 3P_2 state upward relative to their true energies, the correct level energies appear in Fig. 4.

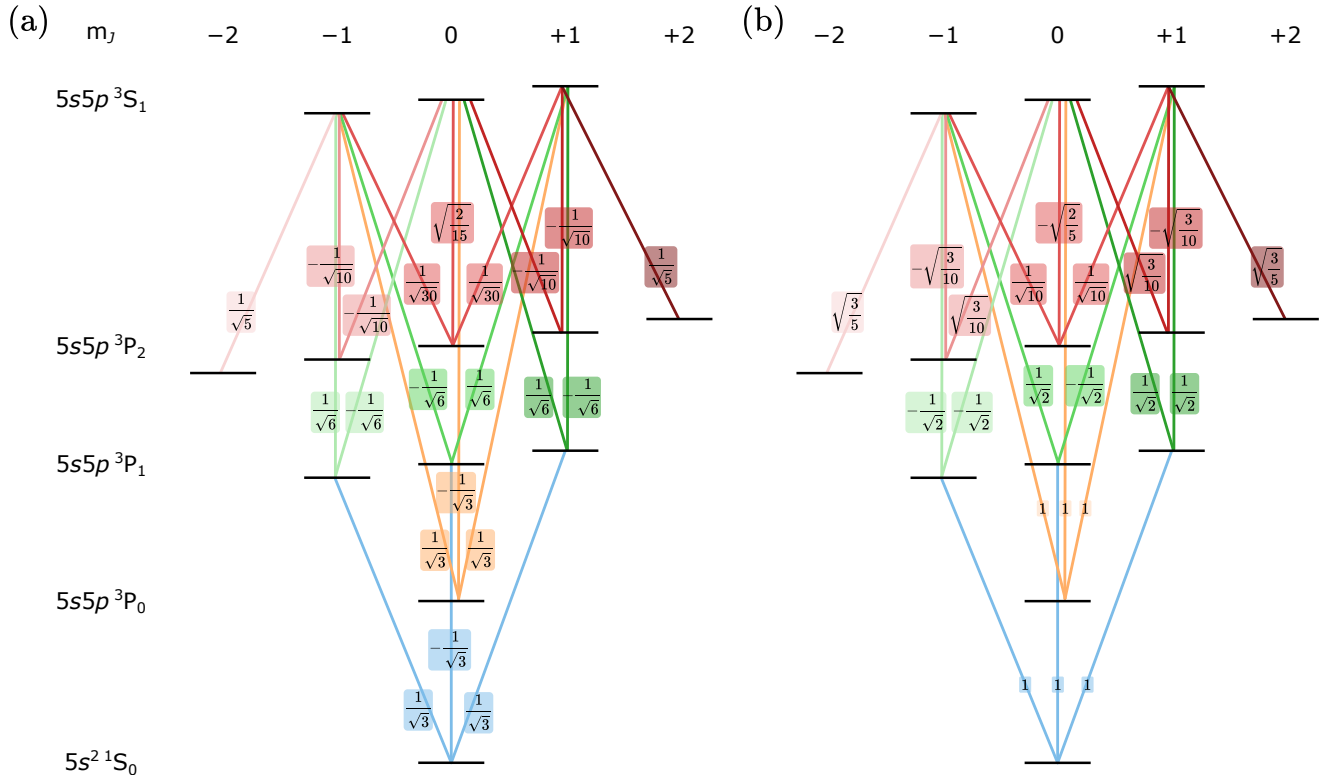


Figure 3: Polarization-dependent coupling factors for the transition between various Zeeman levels. (a) Wigner factors $w_q^{g \rightarrow e}$ as defined in Eq. 65. (b) The corresponding Clebsch-Gordan coefficients $\langle J_g m_{J_g}; 1 q | J_e m_{J_e} \rangle$, given in Eq. 64, for the same set of sublevels and polarizations. Note that a similar figure can be found in Ref. [113].

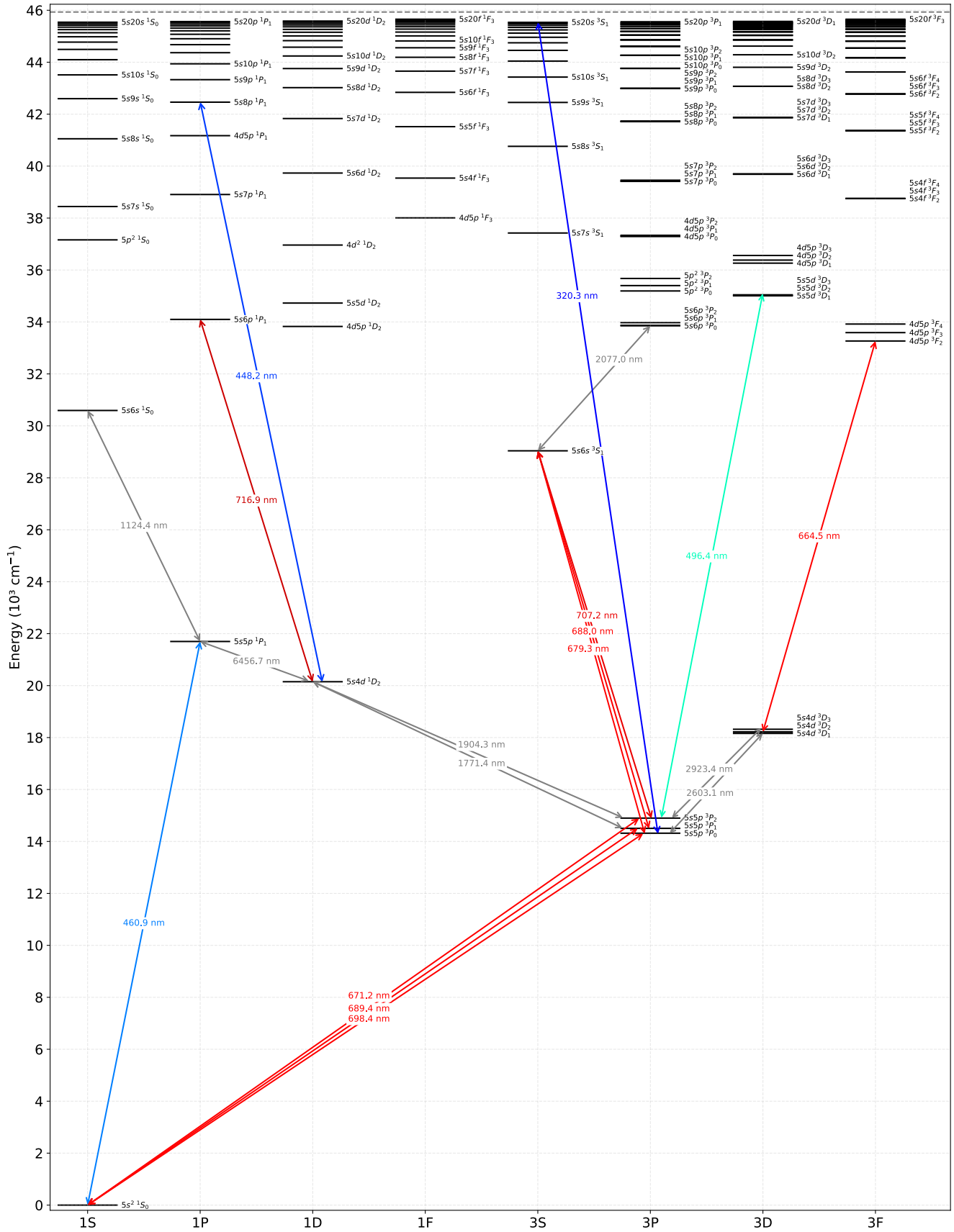


Figure 4: Neutral Sr I energy level diagram with selected optical transitions. Level energies and transition wavelengths are taken from the NIST Atomic Spectra Database [107]. The dashed gray line shows the ionization energy.

9 Acknowledgments

We thank Robin Eberhard, Neven Šantić, and Eric Yilun Song for stimulating discussions, comments, corrections, and suggestions. S.L.K. acknowledges support from the Independent Research Fund Denmark.

References

- [1] D. A. Steck, *Sodium D Line Data*, Available online at <http://steck.us/alkalidata>, Revision 2.3.3, original revision posted 27 May 2000, 2024.
- [2] D. A. Steck, *Rubidium 85 D Line Data*, Available online at <http://steck.us/alkalidata>, Revision 2.3.3, original revision posted 30 April 2008, 2024.
- [3] D. A. Steck, *Rubidium 87 D Line Data*, Available online at <http://steck.us/alkalidata>, Revision 2.3.3, original revision posted 25 September 2001, 2024.
- [4] D. A. Steck, *Cesium D Line Data*, Available online at <http://steck.us/alkalidata>, Revision 2.3.3, original revision posted 23 January 1998, 2024.
- [5] R. T. Birge, “The Calculation of Errors by the Method of Least Squares”, *Physical Review* **40**, 207–227 (1932).
- [6] M. Trassinelli and M. Maxton, “A Minimalistic and General Weighted Averaging Method for Inconsistent Data”, Revised 21 Dec 2024 (v2), 10.48550/arXiv.2406.08293 (2024).
- [7] W. M. Haynes, ed., *CRC Handbook of Chemistry and Physics*, 97th ed., CRC Press (Boca Raton, Florida, 2016), p. 2670.
- [8] P. J. Mohr, D. B. Newell, B. N. Taylor, and E. Tiesinga, “CODATA recommended values of the fundamental physical constants: 2022”, *Rev. Mod. Phys.* **97**, 025002 (2025).
- [9] M. Wang, W. J. Huang, F. G. Kondev, G. Audi, and S. Naimi, “The AME 2020 Atomic Mass Evaluation (II): Tables, Graphs and References”, *Chinese Physics C* **45**, 030003 (2021).
- [10] F. G. Kondev, M. Wang, W. J. Huang, S. Naimi, and G. Audi, “The NUBASE2020 Evaluation of Nuclear Physics Properties”, *Chinese Physics C* **45**, 030001 (2021).
- [11] R. Rana, M. Höcker, and E. G. Myers, “Atomic masses of strontium and ytterbium”, *Physical Review A* **86**, 050502 (2012).
- [12] J. W. Arblaster, *Selected Values of the Crystallographic Properties of the Elements*, ASM International (Materials Park, Ohio, 2018).
- [13] C. B. Alcock, V. P. Itkin, and M. K. Horrigan, “Vapour Pressure Equations for the Metallic Elements: 298–2500K”, *Canadian Metallurgical Quarterly* **23**, 309–313 (1984).
- [14] E. Braaten and H.-W. Hammer, “Universality in Few-Body Systems with Large Scattering Length”, *Physics Reports* **428**, 259–390 (2006).
- [15] C. Chin, R. Grimm, P. Julienne, and E. Tiesinga, “Feshbach resonances in ultracold gases”, *Rev. Mod. Phys.* **82**, 1225–1286 (2010).
- [16] S. Stellmer, “Degenerate Quantum Gases of Strontium”, Dissertation; Institute of Experimental Physics & IQOQI, Austrian Academy of Sciences, (Faculty of Mathematics, Computer Science and Physics, University of Innsbruck, Innsbruck, Austria, Jan. 2013).
- [17] Y. Takasu, Y. Fukushima, Y. Nakamura, and Y. Takahashi, “Magnetoassociation of a Feshbach Molecule and Spin–Orbit Interaction between the Ground and Electronically Excited States”, *Physical Review A* **96**, 023602 (2017).
- [18] J. Samland, “Pumping the Zeeman Slower”, Master’s thesis, (Van der Waals–Zeeman Institute, Institute of Physics, University of Amsterdam, Amsterdam, Netherlands, Apr. 15, 2019).
- [19] F. Wallner, “New Tools for Controlling Strontium Atoms with High Spectral and Spatial Resolution”, Master’s thesis, (Physics Department, Technical University of Munich and Max Planck Institute of Quantum Optics, Munich, Germany, Dec. 15, 2020).
- [20] H. A. Bethe and E. E. Salpeter, *Quantum Mechanics of One- and Two-Electron Atoms*, Springer-Verlag (Berlin, Germany, 1957).

- [21] G. Breit and L. A. Wills, “Hyperfine Structure in Intermediate Coupling”, *Physical Review* **44**, 470 (1933).
- [22] A. Lurio, M. Mandel, and R. Novick, “Second-Order Hyperfine and Zeeman Corrections for an (*sl*) Configuration”, *Physical Review* **126**, 1758 (1962).
- [23] M. M. Boyd, T. Zelevinsky, A. D. Ludlow, S. Blatt, T. Zanon-Willette, S. M. Foreman, and J. Ye, “Nuclear Spin Effects in Optical Lattice Clocks”, *Physical Review A* **76**, 022510 (2007).
- [24] R. Santra, K. V. Christ, and C. H. Greene, “Properties of Metastable Alkaline-Earth-Metal Atoms Calculated Using an Accurate Effective Core Potential”, *Physical Review A* **69**, 042510 (2004).
- [25] M. M. Boyd, “High Precision Spectroscopy of Strontium in an Optical Lattice: Towards a New Standard for Frequency and Time”, PhD thesis, JILA and Department of Physics, (University of Colorado Boulder, Aug. 2007).
- [26] A. V. Taichenachev, V. I. Yudin, C. W. Oates, C. W. Hoyt, Z. W. Barber, and L. Hollberg, “Magnetic Field-Induced Spectroscopy of Forbidden Optical Transitions with Application to Lattice-Based Optical Atomic Clocks”, *Physical Review Letters* **96**, 083001 (2006).
- [27] I. S. Madjarov, “Entangling, controlling, and detecting individual strontium atoms in optical tweezer arrays”, PhD thesis, (California Institute of Technology, Pasadena, California, USA, Jan. 22, 2021).
- [28] B. Edlén, “The Refractive Index of Air”, *Metrologia* **2**, 71–80 (1966).
- [29] E. R. Peck and K. Reeder, “Dispersion of Air”, *Journal of the Optical Society of America* **62**, 958–962 (1972).
- [30] A. L. Buck, “New Equations for Computing Vapor Pressure and Enhancement Factor”, *Journal of Applied Meteorology* **20**, 1527–1532 (1981).
- [31] Buck Research Instruments, LLC, *CR-1A Hygrometer with Autofill: Operating Manual*, Buck Research Instruments, LLC (Boulder, CO, USA, May 2012).
- [32] J. E. Sansonetti and G. Nave, “Wavelengths, Transition Probabilities, and Energy Levels for the Spectrum of Neutral Strontium (Sr I)”, *Journal of Physical and Chemical Reference Data* **39**, 033103 (2010).
- [33] F. J. Sullivan, *Strontium Lines in Arc and Solar Spectra*, 3 (University of Pittsburgh Bulletin, 1936).
- [34] I. Courtillot, A. Quessada-Vial, A. Brusch, D. Kolker, G. D. Rovera, P. Lemonde, et al., “Accurate Spectroscopy of Sr Atoms”, *European Physical Journal D* **33**, 161–171 (2005).
- [35] X. Baillard, M. Fouché, R. Le Targat, P. G. Westergaard, A. Lecallier, Y. Le Coq, G. D. Rovera, S. Bize, and P. Lemonde, “Accuracy evaluation of an optical lattice clock with bosonic atoms”, *Opt. Lett.* **32**, 1812–1814 (2007).
- [36] P. Morzyński, M. Bober, D. Bartoszek-Bober, J. Nawrocki, P. Krehlik, L. Śliwczynski, M. Lipiński, P. Masłowski, A. Cygan, P. Dunst, M. Garuś, D. Lisak, J. Zachorowski, W. Gawlik, C. Radzewicz, R. Ciuryło, and M. Zawada, “Absolute measurement of the 1S_0 – 3P_0 clock transition in neutral ^{88}Sr over the 330 km-long stabilized fibre optic link”, *Scientific Reports* **5**, 17495 (2015).
- [37] Bureau International des Poids et Mesures (BIPM), *Recommended Value of the Frequency of the $^1S_0 \rightarrow ^3P_0$ Transition of ^{88}Sr* , (2021) https://www.bipm.org/documents/20126/69375105/88Sr_429THz_2021.pdf/fc359ab2-0e0f-5345-fd69-ba7d1a1b7327 (visited on 05/25/2025).
- [38] Consultative Committee for Time and Frequency (CCTF), *Recommendation PSFS-2*, 22nd meeting (session II – online), (2021) <https://www.bipm.org/en/committees/cc/cctf/22-2-2021> (visited on 05/21/2025).
- [39] J. Trautmann, D. Yankelev, V. Klüsener, A. J. Park, I. Bloch, and S. Blatt, “The 1S_0 – 3P_2 Magnetic Quadrupole Transition in Neutral Strontium”, *Physical Review Research* **5**, 013219 (2023).
- [40] O. Onishchenko, S. Pyatchenkov, A. Urech, C.-C. Chen, S. Bennetts, G. A. Siviloglou, and F. Schreck, “Frequency of the Ultranarrow $^1S_0 \rightarrow ^3P_2$ Transition in ^{87}Sr ”, *Physical Review A* **99**, 052503 (2019).
- [41] S. M. Heider and G. O. Brink, “Hyperfine Structure of ^{87}Sr in the 3P_2 Metastable State”, *Physical Review A* **16**, 1371–1374 (1977).
- [42] A. Heinz, A. J. Park, N. Šantić, J. Trautmann, S. G. Porsev, M. S. Safronova, I. Bloch, and S. Blatt, “State-Dependent Optical Lattices for the Strontium Optical Qubit”, *Physical Review Letters* **124**, 203201 (2020).
- [43] I. Puljić, A. Cipriš, D. Aumiler, T. Ban, and N. Šantić, “Lifetime measurement of the $5s5p\ ^1P_1$ state in strontium”, *Phys. Rev. A* **111**, 032809 (2025).
- [44] A. Lurio, R. L. de Zafra, and R. J. Goshen, “Lifetime of the First 1P_1 State of Zinc, Calcium, and Strontium”, *Physical Review* **134**, A1198 (1964).

- [45] F. M. Kelly and M. S. Mathur, “Hanle effect in the singlet excited states of the alkaline earths”, *Canadian Journal of Physics* **58**, 1416–1419 (1980).
- [46] S. B. Nagel, P. G. Mickelson, A. D. Saenz, Y. N. Martinez, Y. C. Chen, T. C. Killian, P. Pellegrini, and R. Côté, “Photoassociative Spectroscopy at Long Range in Ultracold Strontium”, *Physical Review Letters* **94**, 083004 (2005).
- [47] M. Yasuda, T. Kishimoto, M. Takamoto, and H. Katori, “Photoassociation Spectroscopy of Strontium: Reconstruction of the Wave Function Near the Last Node”, *Physical Review A* **73**, 011403(R) (2006).
- [48] P. Barakhshan, A. Marrs, A. Bhosale, B. Arora, R. Eigenmann, and M. S. Safronova, *Portal for High-Precision Atomic Data and Computation (version 2.0)*, University of Delaware, Newark, DE, USA. <https://www.udel.edu/atom>, Accessed May 25, 2025. Original data source cited where available. 2022.
- [49] A. Cooper, J. P. Covey, I. S. Madjarov, S. G. Porsev, M. S. Safronova, and M. Endres, “Alkaline-Earth Atoms in Optical Tweezers”, *Physical Review X* **8**, 041055 (2018).
- [50] D. Husain and G. Roberts, “Radiative Lifetimes, Diffusion and Energy Pooling of $\text{Sr}(5s5p\ (^3P_J))$ and $\text{Sr}(5s4d\ (^1D_2))$ Studied by Time-Resolved Atomic Emission Following Pulsed Dye-Laser Excitation”, *Chemical Physics* **127**, 203–225 (1988).
- [51] D. S. Barker, B. J. Reschovsky, N. C. Pienti, and G. K. Campbell, “Enhanced Magnetic Trap Loading for Atomic Strontium”, *Physical Review A* **92**, 043418 (2015).
- [52] X. Xu, T. H. Loftus, J. L. Hall, A. Gallagher, and J. Ye, “Cooling and Trapping of Atomic Strontium”, *Journal of the Optical Society of America B* **20**, 968–976 (2003).
- [53] J. Bauschlicher C. W., S. R. Langhoff, and H. Partridge, “The Radiative Lifetime of the 1D_2 State of Ca and Sr: A Core-Valence Treatment”, *Journal of Physics B: Atomic and Molecular Physics* **18**, 1523 (1985).
- [54] T. L. Nicholson, S. L. Campbell, R. B. Hutson, G. E. Marti, B. J. Bloom, R. L. McNally, W. Zhang, M. D. Barrett, M. S. Safronova, G. F. Strouse, W. L. Tew, and J. Ye, “Systematic Evaluation of an Atomic Clock at 2×10^{-18} Total Uncertainty”, *Nature Communications* **6**, 6896 (2015).
- [55] M. D. Havey, L. C. Balling, and J. J. Wright, “Measurement of the 3P_1 Lifetime in Sr”, *Physical Review A* **13**, 1269 (1976).
- [56] R. Drozdowski, M. Ignaciuk, J. Kwela, and J. Heldt, “Radiative Lifetimes of the Lowest 3P_1 Metastable States of Ca and Sr”, *Zeitschrift für Physik D: Atoms, Molecules and Clusters* **41**, 125–131 (1997).
- [57] I.-J. Ma, G. zu Putlitz, and G. Schütte, “Lebensdauer des $5s\ 5p\ ^3P_1$ -Zustands von Strontium”, *Zeitschrift für Physik A: Hadrons and Nuclei* **208**, 276–285 (1968).
- [58] U. Brinkmann, “Lifetimes and Oscillator Strengths in the Sr I and Ca I Spectra”, *Zeitschrift für Physik* **228**, 440–453 (1969).
- [59] M. D. Havey, L. C. Balling, and J. J. Wright, “Direct Measurements of Excited-State Lifetimes in Mg, Ca, and Sr”, *Journal of the Optical Society of America* **67**, 488–491 (1977).
- [60] G. Jönsson, C. Levinson, A. Persson, and C.-G. Wahlström, “Natural Radiative Lifetimes in the 1P_1 and 1F_3 Sequences of Sr I”, *Zeitschrift für Physik A: Atoms and Nuclei* **316**, 255–258 (1984).
- [61] V. Klüsener, S. Pucher, D. Yankelev, J. Trautmann, F. Spriestersbach, D. Filin, S. G. Porsev, M. S. Safronova, I. Bloch, and S. Blatt, “Long-Lived Coherence on a μHz Scale Optical Magnetic Quadrupole Transition”, *Physical Review Letters* **132**, 253201 (2024).
- [62] A. Derevianko, “Feasibility of Cooling and Trapping Metastable Alkaline-Earth Atoms”, *Physical Review Letters* **87**, 023002 (2001).
- [63] M. Yasuda and H. Katori, “Lifetime Measurement of the Metastable State of Strontium Atoms”, *Physical Review Letters* **92**, 153004 (2004).
- [64] A. Corney, *Atomic and Laser Spectroscopy*, 1st ed., Clarendon Press, Oxford University Press (Oxford, United Kingdom, 1977).
- [65] W. Demtröder, *Laser Spectroscopy: Volume 1: Basic Principles*, 4th ed., Springer-Verlag (Berlin Heidelberg, 2008).
- [66] P. D. Lett, R. N. Watts, C. I. Westbrook, W. D. Phillips, P. L. Gould, and H. J. Metcalf, “Observation of Atoms Laser Cooled below the Doppler Limit”, *Physical Review Letters* **61**, 169–172 (1988).

- [67] M. Schioppo, N. Poli, M. Prevedelli, S. Falke, C. Lisdat, U. Sterr, and G. M. Tino, “A compact and efficient strontium oven for laser-cooling experiments”, *Review of Scientific Instruments* **83**, 103101 (2012).
- [68] P. G. Mickelson, Y. N. Martínez de Escobar, P. Anzel, B. J. DeSalvo, S. B. Nagel, A. J. Traverso, M. Yan, and T. C. Killian, “Repumping and Spectroscopy of Laser-Cooled Sr Atoms Using the $(5s5p) {}^3P_2 \rightarrow (5s4d) {}^3D_2$ Transition”, *Journal of Physics B: Atomic, Molecular and Optical Physics* **42**, 235001 (2009).
- [69] S. Stellmer and F. Schreck, “Reservoir spectroscopy of $5s5p {}^3P_2$ – $5snd {}^3D_{1,2,3}$ transitions in strontium”, *Phys. Rev. A* **90**, 022512 (2014).
- [70] S. B. Nagel, “Ultracold collisions in atomic strontium”, PhD thesis, (Rice University, Houston, TX, Feb. 2008).
- [71] S. B. Nagel, C. E. Simien, S. Laha, P. Gupta, V. S. Ashoka, and T. C. Killian, “Magnetic trapping of metastable 3P_2 atomic strontium”, *Physical Review A* **67**, 011401 (2003).
- [72] H. Katori, T. Ido, Y. Isoya, and M. Kuwata-Gonokami, “Magneto-Optical Trapping and Cooling of Strontium Atoms down to the Photon Recoil Temperature”, *Physical Review Letters* **82**, 1116 (1999).
- [73] R. González Escudero, “Magnetic field control and laser frequency stabilization for strontium magneto-optical traps”, Master’s thesis, (Fakultät für Physik, Ludwig-Maximilians-Universität München and Max-Planck-Institut für Quantenoptik, München, Germany, Sept. 15, 2016).
- [74] M. A. Norcia, “New Tools for Precision Measurement and Quantum Science with Narrow-Linewidth Optical Transitions”, PhD thesis, (University of Colorado, Boulder (JILA), Boulder, CO, USA, 2019).
- [75] S. L. Kristensen, “Narrow-Linewidth Superradiant Lasing with Cold ${}^{88}\text{Sr}$ Atoms”, PhD thesis, (Niels Bohr Institute, University of Copenhagen, Copenhagen, Denmark, Dec. 2023).
- [76] S. Stellmer, R. Grimm, and F. Schreck, “Production of Quantum-Degenerate Strontium Gases”, *Physical Review A* **87**, 013611 (2013).
- [77] T. H. Loftus, T. Ido, A. D. Ludlow, M. M. Boyd, and J. Ye, “Narrow Line Cooling: Finite Photon Recoil Dynamics”, *Physical Review Letters* **93**, 073003 (2004).
- [78] I. V. Hertel and C.-P. Schulz, *Atoms, Molecules and Optical Physics 2: Molecules and Photons – Spectroscopy and Collisions*, 1st ed., Vol. 2, Graduate Texts in Physics, Springer Berlin Heidelberg (Berlin, Heidelberg, 2015).
- [79] R. Grimm, M. Weidemüller, and Y. B. Ovchinnikov, “Optical Dipole Traps for Neutral Atoms”, in *Advances in Atomic, Molecular, and Optical Physics*, Vol. 42 (Academic Press, 2000), pp. 95–170.
- [80] F. Le Kien, P. Schneeweiss, and A. Rauschenbeutel, “Dynamical polarizability of atoms in arbitrary light fields: general theory and application to cesium”, *The European Physical Journal D* **67**, 92 (2013).
- [81] V. V. Tsyganok, D. A. Pershin, E. T. Davletov, V. A. Khlebnikov, and A. V. Akimov, “Scalar, Tensor, and Vector Polarizability of Tm Atoms in a 532-nm Dipole Trap”, *Physical Review A* **100**, 042502 (2019).
- [82] P. Barakhshan, A. Bhosale, A. Kiruga, R. Eigenmann, M. S. Safronova, and B. Arora, “A Portal for High-Precision Atomic Data and Computation: Design and Best Practices”, *arXiv preprint*, 10.48550/arXiv.2212.10665 (2022).
- [83] T. Ido and H. Katori, “Recoil-Free Spectroscopy of Neutral Sr Atoms in the Lamb-Dicke Regime”, *Physical Review Letters* **91**, 053001 (2003).
- [84] M. A. Norcia, A. W. Young, and A. M. Kaufman, “Microscopic Control and Detection of Ultracold Strontium in Optical-Tweezer Arrays”, *Physical Review X* **8**, 041054 (2018).
- [85] G. Kestler, K. Ton, D. Filin, M. S. Safronova, and J. T. Barreiro, “Magic Wavelengths of the Sr $(5s^2 {}^1S_0 - 5s5p {}^3P_1)$ Intercombination Transition near the $5s5p {}^3P_1 - 5p^2 {}^3P_2$ Transition”, *Physical Review A* **105**, 012821 (2022).
- [86] G. Kestler, K. Ton, D. Filin, C. Cheung, P. Schneeweiss, T. Hoinkes, J. Volz, M. S. Safronova, A. Rauschenbeutel, and J. T. Barreiro, “State-Insensitive Trapping of Alkaline-Earth Atoms in a Nanofiber-Based Optical Dipole Trap”, *PRX Quantum* **4**, 040308 (2023).
- [87] M. Takamoto, H. Katori, S. I. Marmo, V. D. Ovsiannikov, and V. G. Pal’chikov, “Prospects for Optical Clocks with a Blue-Detuned Lattice”, *Physical Review Letters* **102**, 063002 (2009).
- [88] X. Ma, S. Das, D. Wilkowski, and C. C. Kwong, “Magic Wavelength at 477 nm for the Strontium Clock Transition”, *arXiv preprint*, 10.48550/arXiv.2507.04532 (2025).

- [89] G. Kestler, R. J. Sedlik, E. C. Trapp, M. S. Safronova, and J. T. Barreiro, “Turquoise Magic Wavelength of the ^{87}Sr Clock Transition”, arXiv preprint, 10.48550/arXiv.2506.18958 (2025).
- [90] M. Takamoto, F.-L. Hong, R. Higashi, and H. Katori, “An Optical Lattice Clock”, *Nature* **435**, 321–324 (2005).
- [91] T. Akatsuka, M. Takamoto, and H. Katori, “Three-Dimensional Optical Lattice Clock with Bosonic Atoms”, *Physical Review A* **81**, 023402 (2010).
- [92] Q. Wang, Y.-G. Lin, F. Meng, Y. Li, B.-K. Lin, E.-J. Zang, T.-C. Li, and Z.-J. Fang, “Magic Wavelength Measurement of the ^{87}Sr Optical Lattice Clock at NIM”, *Chinese Physics Letters* **33**, 103201 (2016).
- [93] M. Ammenwerth, H. Timme, F. Gyger, R. Tao, I. Bloch, and J. Zeiher, “Realization of a Fast Triple-Magic All-Optical Qutrit in Strontium-88”, 10.48550/arXiv.2411.02869 (2024).
- [94] S. Pucher, V. Klüsener, F. Priestersbach, J. Geiger, A. Schindewolf, I. Bloch, and S. Blatt, “Fine-Structure Qubit Encoded in Metastable Strontium Trapped in an Optical Lattice”, *Physical Review Letters* **132**, 150605 (2024).
- [95] M. Auzinsh, D. Budker, and S. Rochester, *Optically Polarized Atoms: Understanding Light–Atom Interactions* (Oxford University Press, Oxford, United Kingdom, 2010).
- [96] S. Origlia, M. S. Pramod, S. Schiller, Y. Singh, K. Bongs, R. Schwarz, A. Al-Masoudi, S. Dörscher, S. Herbers, S. Häfner, U. Sterr, and C. Lisdat, “Towards an Optical Clock for Space: Compact, High-Performance Optical Lattice Clock Based on Bosonic Atoms”, *Physical Review A* **98**, 053443 (2018).
- [97] C. J. Foot, *Atomic Physics* (Oxford University Press, Oxford, United Kingdom, 2004).
- [98] I. Angeli and K. P. Marinova, “Table of experimental nuclear ground state charge radii: An update”, *Atomic Data and Nuclear Data Tables* **99**, 69–95 (2013).
- [99] J. R. Rubbmark and S. A. Borgström, “Rydberg Series in Strontium Found in Absorption by Selectively Laser-Excited Atoms”, *Physica Scripta* **18**, 196–208 (1978).
- [100] Y. N. Martínez de Escobar, P. G. Mickelson, P. Pellegrini, S. B. Nagel, A. Traverso, M. Yan, R. Côté, and T. C. Killian, “Two-Photon Photoassociative Spectroscopy of Ultracold $^{88}\text{Sr}_2$ ”, *Physical Review A* **78**, 062708 (2008).
- [101] A. Stein, H. Knöckel, and E. Tiemann, “Fourier-Transform Spectroscopy of Sr_2 and Revised Ground-State Potential”, *Physical Review A* **78**, 042508 (2008).
- [102] A. Stein, H. Knöckel, and E. Tiemann, “The $^1S + ^1S$ Asymptote of Sr_2 Studied by Fourier-Transform Spectroscopy”, *European Physical Journal D* **57**, 171–177 (2010).
- [103] P. G. Mickelson, Y. N. Martínez de Escobar, A. D. Saenz, S. B. Nagel, Y. C. Chen, T. C. Killian, P. Pellegrini, and R. Côté, “Spectroscopic Determination of the s-Wave Scattering Lengths of ^{86}Sr and ^{88}Sr ”, *Physical Review Letters* **95**, 223002 (2005).
- [104] G. Ferrari, R. E. Drullinger, N. Poli, F. Sorrentino, and G. M. Tino, “Cooling of Sr to High Phase-Space Density by Laser and Sympathetic Cooling in Isotopic Mixtures”, *Physical Review A* **73**, 023408 (2006).
- [105] M. Witkowski, S. Bilicki, M. Bober, D. Kovačić, V. Singh, A. Tonoyan, and M. Zawada, “Photoionization Cross Sections of Ultracold ^{88}Sr in 1P_1 and 3S_1 States at 390 nm and the Resulting Blue-Detuned Magic Wavelength Optical Lattice Clock Constraints”, *Optics Express* **30**, 21423–21438 (2022).
- [106] G. Unnikrishnan, P. Ilzhöfer, A. Scholz, C. Hölzl, A. Götzelmann, R. K. Gupta, J. Zhao, J. Krauter, S. Weber, N. Makki, H. P. Büchler, T. Pfau, and F. Meinert, “Coherent Control of the Fine-Structure Qubit in a Single Alkaline-Earth Atom”, *Physical Review Letters* **132**, 150606 (2024).
- [107] A. Kramida, Y. Ralchenko, J. Reader, and N. A. Team, *NIST Atomic Spectra Database (ver. 5.12)*, Online at <https://physics.nist.gov/PhysRefData/ASD/> [Accessed June 1, 2025], 2024.
- [108] B. Bushaw and W. Nörtershäuser, “Resonance Ionization Spectroscopy of Stable Strontium Isotopes and ^{90}Sr via $5s^2\ ^1S_0 \rightarrow 5s5p\ ^1P_1 \rightarrow 5s5d\ ^1D_2 \rightarrow 5s11f\ ^1F_3 \rightarrow \text{Sr}^+$ ”, *Spectrochimica Acta Part B: Atomic Spectroscopy* **55**, 1679–1692 (2000).
- [109] C. Zhang, R. Terabayashi, and S. Hasegawa, “Investigation of Isotope Shifts and Stark Shifts in the Strontium Rydberg State via $5s^2\ ^1S_0 \rightarrow 5s5p\ ^1P_1 \rightarrow 5p^{1/2} \rightarrow 4d^{3/2}\text{ nljn}^* = 39.4$ ”, *Spectrochimica Acta Part B: Atomic Spectroscopy* **225**, 107118 (2025).

- [110] G. Ferrari, P. Cancio, R. Drullinger, G. Giusfredi, N. Poli, M. Prevedelli, C. Toninelli, and G. M. Tino, “Precision Frequency Measurement of Visible Intercombination Lines of Strontium”, *Physical Review Letters* **91**, 243002 (2003).
- [111] H. Miyake, N. C. Pienti, P. K. Elgee, A. Sitaram, and G. K. Campbell, “Isotope-Shift Spectroscopy of the $^1S_0 \rightarrow ^3P_1$ and $^1S_0 \rightarrow ^3P_0$ Transitions in Strontium”, *Physical Review Research* **1**, 033113 (2019).
- [112] T. Takano, R. Mizushima, and H. Katori, “Precise Determination of the Isotope Shift of ^{88}Sr – ^{87}Sr Optical Lattice Clock by Sharing Perturbations”, *Applied Physics Express* **10**, 072801 (2017).
- [113] M. Tang, “Superradiant Lasers Based on Strontium-88”, PhD thesis, (Niels Bohr Institute, Copenhagen, Denmark, Nov. 2022).